Understanding Environmental Stability of Two-Dimensional Materials And Extending Their Shelf Life by Surface Functionalization

by

Sijie Yang

A Dissertation Presented in Partial Fulfillment
of the Requirements for the Degree
Doctor of Philosophy

Approved November 2017 by the
Graduate Supervisory Committee:

Ian Gould, Co-Chair
Sefaattin Tongay, Co-Chair
Ryan Trovitch
Giovanna Ghirlanda

ARIZONA STATE UNIVERSITY

December 2017

ABSTRACT

Since the discovery of graphene, two dimensional materials (2D materials) have become a focus of interest for material research due to their many unique physical properties embedded in their 2D structure. While they host many exciting potential applications, some of these 2D materials are subject to environmental instability issues induced by interaction between material and gas molecules in air, which poses a barrier to further application and manufacture. To overcome this, it is necessary to understand the origin of material instability and interaction with molecules commonly found in air, as well as developing a reproducible and manufacturing compatible method to post-process these materials to extend their lifetime. In this work, the very first investigation on environmental stability on Te containing anisotropic 2D materials such as GaTe and $ZrTe_3$ is reported. Experimental results have demonstrated that freshly exfoliated GaTe quickly deteriorate in air, during which the Raman spectrum, surface morphology, and surface chemistry undergo drastic changes. Environmental Raman spectroscopy and XPS measurements demonstrate that H_2O molecules in air interact strongly on the surface while O_2, N_2, and inert gases don't show any detrimental effects on GaTe surface. Moreover, the anisotropic properties of GaTe slowly disappear during the aging process. To prevent this gas/material interaction based surface transformation, diazonium based surface functionalization is adopted on these Te based 2D materials. Environmental Raman spectroscopy results demonstrate that the stability of functionalized Te based 2D materials exhibit much higher stability both in ambient and extreme conditions. Meanwhile, PL spectroscopy, angle resolved Raman spectroscopy, atomic force microscopy measurements confirm that many attractive physical properties of the

material are not affected by surface functionalization. Overall, these findings unveil the degradation mechanism of Te based 2D materials as well as provide a way to significantly enhance their environmental stability through an inexpensive and reproducible surface chemical functionalization route.

DEDICATION

I dedicate this work to my father and mother, for without their early guidance and constant support, nothing I did would have been achieved.

ACKNOWLEDGMENTS

Firstly, I would like to express my most sincere gratitude to my advisor, Prof. Sefaattin Tongay for the constant support of my Ph.D study and research, for his immense knowledge, motivation, enthusiasm, and patience. His guidance helped me throughout my research and writing of this thesis. I could not have imagined a more supportive advisor and mentor for my Ph.D study.

I would also like to thank the rest of my thesis committee: Prof. Ian Gould, Prof Ryan Trovitch, and Prof. Giovanna Ghirlanda, for their insightful comments, encouragement, and professional questions that incented me to broaden my research from various aspects.

My sincere thanks go to Dr. V. Ongun Özçelik and Dr. Claire E. White from Princeton University for their timely support of meticulous theoretical calculations. I would also like to thank Dr. D. Frank Ogletree from Lawrence Berkeley National Laboraroty for his help with XPS measurements. My thanks also go to Bin Chen, who has been assisting with extensive AFM measurements, and to Meng Wang, who contributed intensively in the organic synthesis, without whom the synthesis would never have been achieved.

I thank my fellow labmates in Dr. Tongay's group at Arizona State University: Dr. Aslihan Tuna, Dr. Yuxia Shen, Hui Cai, Bin Chen, Kedi Wu, Amm Hasib, Ying Qin, Yi Zhou, Han, Li, Anupum Punt, Xi Fan, Ashutosh Aggrawal, and Wilson Kong, for their direct and indirect contributions to this project.

Last but not the least, I would like to thank my family, my parents Jiaqing Yang and Juhua Xu, for their support in every way through my life that made this work possible.

TABLE OF CONTENTS

Page

LIST OF FIGURES ix

CHAPTER

1 INTRODUCTION TO 2D MATERIALS 1

1.1 Basics of 2D Materials 1

1.1.1 What Are 2D Materials 1

1.1.2 What Do 2D Materials Offer 1

1.2 Types of 2D Materials 2

1.2.1 Dichalcogenides 2

1.2.2 Monochalcogenides 3

1.2.3 Trichalcogenides 4

2 NOVEL CHARACTERIZATION TECHNIQUES FOR 2D MATERIALS 6

2.1 Need for Novel Characterization Techniques 6

2.2 Characterization Techniques for 2D Materials 6

2.2.1 Raman Spectroscopy 6

2.2.2 Photoluminescence Spectroscopy 12

2.2.3 Atomic Force Microscopy 18

3 SYNTHESIS OF NOVEL 2D MATERIALS 22

3.1 Isolation of Monolayers from Bulk Crystals 22

3.1.1 Mechanical Exfoliation 22

3.1.2 Bulk Crystal Growth 23

3.2 Chemical/Physical Vapor Deposition Techiniques 24
3.2.1 MoS_2 Growth 28
4 UNDERSTANDING ENVIRONMENTAL STABILITY OF TE BASED 2D MATERIALS 29
4.1 Degradation of Te Based 2D Materials 29
4.2 Investigating Environmental Degradation 30
4.2.1 Design of Experiments 30
4.2.2 Interaction with Gas Molecules in Air 32
4.2.3 Anisotropic to Isotropic Transition 35
4.2.4 Surface Morphology Changes 37
4.3 Summary 40
5 EXTENDING SHELF LIFE OF 2D MATERIALS 41
5.1 General Route to Material Stabilization 42
5.2 Results of Surface Functionalization 43
5.2.1 Enhanced Material Stability 43
5.2.2 Effects on Surface Morphology 45
5.2.3 Unaffected Physical Properties 46
5.3 Summary 50
6 STABILITY OF HEXAAMINOBENZENE BASED 2D POLYMERS 51
6.1 Introduction to 2D Polymers 51
6.2 Polymer Synthesis 52
6.2.1 Synthesis of Hexaaminobenzene 52
6.2.1.1 Synthesis of TNA 53

6.2.1.2 Synthesis of TATB 54
6.2.1.3 Synthesis of HAB 55
6.2.2 Preparation of HAB Based 2D Polymer 56
6.2.3 Characterization of HAB Based 2D Polymer 57
6.3 Environmental Stability of HAB Based 2D Polymer 60
6.3.1 Laser Induced Degradation.....60
6.3.2 Thermal Stability 61
6.4 Future Directions.....62
6.4.1 Further Understanding of Polymer Degradation 62
6.4.2 Improving Polymer Stability 63
REFERENCES.....64

LIST OF FIGURES

Figure Page

1. Side View of Hexagonal WS_2 and Triclinic ReS_2 3
2. Side View of Hexagonal GaSe and Monoclinic GaTe 4
3. Rayleigh and Raman Scattering in a Single Molecule 7
4. Illustration of Raman Scattering 9
5. Raman Spectra of Bi_2Se_3 Recorded with Different Experimental Setups 10
6. Formation of Bands in Solids 13
7. Interband Transition in Direct Band Gap and Indirect Band Gap Materials..... 15
8. Schematics of Photoluminescence in Semiconductors 17
9. Schematics of an Atomic Force Microscope 19
10. Schematics of Mechanical Exfoliation with Tape 22
11. Schematics of Chemical Vapor Transport 23
12. Examples of CVT Ampoules Before and After Growth 24
13. Schematic of Vapor Deposition Process 25
14. Schematic of Boundary Layer in a Laminar Flow System 26
15. Basic Characterization of Monoclinic GaTe 31
16. Environmental and Laser Induced Aging of GaTe 33
17. Insight of Environmental and Laser Induced Aging of GaTe 34
18. Angle Resolved Raman Spectra of GaTe During Environmental Aging 36
19. Surface Degradation Effects of GaTe 38
20. Environmental XPS and I/V Measurements on As-Cleaved and Aged GaTe 39
21. Degradation and Functionalization Schematics 42

22. Effects of Surface Functionalization on GaTe, $ZrTe_3$, and $MoTe_2$ 44
23. Enhanced Stability of Functionalized GaTe in Water 45
24. Surface Morphology and Thickness Changes 46
25. Effects of Surface Functionalization on Physical Properties 48
26. Electronic Effects of Surface Aryl Functionalization 49
27. Synthesis Scheme of Hexaaminobenzene 52
28. ^{1}HNMR and ^{13}CNMR of TNA in DMSO-d6 54
29. ^{13}CNMR of TATB in DMSO-d6 55
30. ^{1}HNMR of HAB in D_2O 56
31. Schematics of 2D Polymer Synthesis 57
32. Morphology Characterization of HAB Based 2D Polymer 58
33. EDX, Raman, and FTIR Spectra of HAB Based 2D Polymer 59
34. Laser Induced Degradation of HAB Based 2D Polymer 60
35. Optical Images of HAB Based 2D Polymer During Thermal Degradation 62

CHAPTER 1

INTRODUCTION TO 2D MATERIALS

1.1 Basics of two dimensional materials

1.1.1 What are two dimensional materials

Two-dimensional (2D) material is defined as crystalline layered materials consisting of atomically thin sheets[1, 2]. Atoms form covalent bonds with each other within the layer, whereas the interaction between layers consists of Van der Waals forces. Existence of such layered materials has been reported decades ago, and the discovery of graphene in 2004 has drawn the attention of researchers on 2D materials due to the unique physical properties possessed by graphene[3, 4]. There exist many different types of 2D materials, including allotropes of a single element such as graphene[3, 4] and black phosphorus[5, 6], as well as many binary compounds such as hexagonal boron nitride[7] (hBN) and transition metal chalcogenides[8, 9]. The structure of 2D materials gives rise to many unusual properties compared to their 3D counterparts, which will be discussed in the following section.

1.1.2 What do 2D materials offer

The physical properties of a material are determined by its structure. When a 3D material is thinned down to two dimensions, heat and charge transport within the material is limited within the plane. This limit in charge transport can result in significant change in the electronic band structure of a material[10]. For example, a layered transition metal dichalcogenide, MoS_2, has an indirect band gap in bulk form. When this material is thinned down to few layers without any structural change within each layer, its band gap becomes direct, which makes the material highly luminescent[11]. Other than MoS_2, this

indirect to direct transition in band gap has been observed in some other layered materials such as $MoSe_2$[10], WS_2[12], and WSe_2[12]. Moreover, some physical properties such as photoluminescence display a strong dependence on the number of layers which has been theoretically predicted and experimentally observed[13]. Meanwhile, when the thickness of 2D material is down to monolayer, its electronical properties become sensitive to the surrounding environment such as substrate and capping material[14], which allows for easy engineering of material properties.

Since the interaction between adjacent layers in a 2D material is Van der Waals force, the material can be easily cleaved down to monolayer form. The monolayers can then be stacked on top of each other to form Van der Waals heterostructures[15] (with monolayer materials of different types). This allows for fabrication of novel nanoscale devices from components with a wide range of electronic properties.

1.2 Types of 2D materials

1.2.1 Dichalcogenides

Dichalcogenides refer to transition metal dichalcogenides (TMDCs) in which a transition metal atom (Ti, Mo, W, Re, etc.) is sandwiched between two chalcogen atoms (S, Se, Te) to form a layered structure. Depending on the identity of metal and chalcogen atoms, the structure of the resulting TMDC could vary greatly. For instance, MoS_2 and WS_2 crystallize in hexagonal structure[12, 13], whereas ReS_2 crystallizes in triclinic structure[16]. The difference in elemental composition and crystal structure of TMDCs gives rise to a broad range of physical properties possessed by these materials. For instance, typical band gaps of TMDCs range from 0.3 eV to 2.0 eV[17]. As mentioned in

the previous section, many of these TMDCs exhibit a tunable band gap with an indirect to direct transition when the thickness of the material is thinned down to monolayer[18].

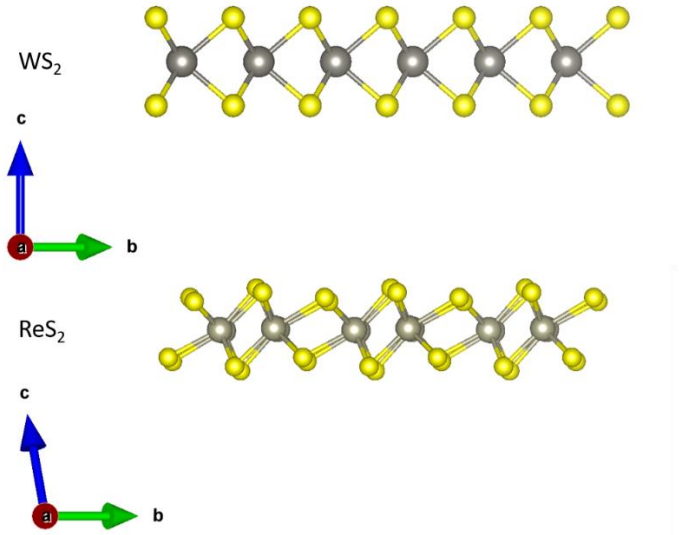

Figure 1.1 Side view of hexagonal WS_2 and triclinic ReS_2.

Owing to their unique physical properties, applications of TMDCs have been developed in many different fields. For example, monolayer MoS_2 has been fabricated into field effect transistors[19, 20] with a high on/off ratio while the material is highly scalable. Other applications of MoS_2 include, but are not limited to, photocatalysis for water splitting[21], biosensors[20], and photodetectors[22, 23].

1.2.2 Monochalcogenides

Monochalcogenides, or more specifically, post-transition metal monochalcogenides (PTMCs), are compounds between a post-transition metal (Ga, Ge, In, etc.) and chalcogen at 1:1 stoichiometry with a layered structure. Within each layer, the atoms are arranged in an X-M-M-X pattern when viewed from the lateral direction[24], with the exception of GaTe, in which the large radius of Te atoms cause a decrease in lattice symmetry. Unlike GaS and GaSe that have hexagonal lattice structure, GaTe

crystallizes in monoclinic phase with Te chains along the *b*-axis direction[25, 26]. The presence of Te chains introduce crystalline anisotropy in monoclinic GaTe. Therefore, monoclinic GaTe is also referred to pseudo-1D material.

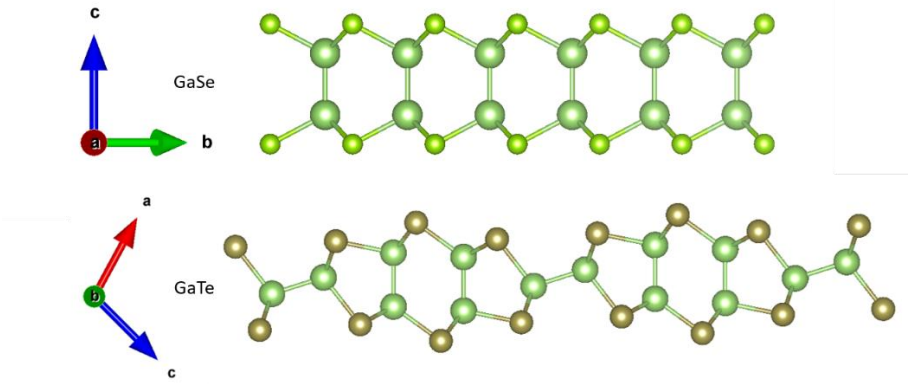

Figure 1.2 Side view of (top) hexagonal GaSe and (bottom) monoclinic GaTe

Among all PTMCs, GaTe is of particular interest because of its pseudo-1D structure. Recent studies on GaTe have proved its vibrational and optical anisotropy as predicted[27]. However, although it has been widely accepted that each layer in 2D material is self-passivated due to no presence of dangling bonds, there are growing concerns on the stability of a few Te containing 2D materials[28, 29], including GaTe. This thesis covers understanding the origin of instability of GaTe and developing a post-processing method to enhance its environmental stability.

1.2.3 Trichalcogenides

Transition metal trichalcogenides (TMTCs) refer to materials that have a common formula of MX_3 where M is a group 4 or 5 transition metal and X is a chalcogen atom (S, Se, and Te)[30]. Like TMDCs and PTMCs, TMTCs also form layered structures with strong covalent bonding within each layer and weak Van der Waals interaction between layers.

However, the covalent bond strength along the *b*-axis direction is stronger compared to covalent bond strength along the *a*-axis direction, resulting in the formation of chain-like features[31]. Because of this, TMTC materials also fall into the category of pseudo-1D materials and they are excepted to exhibit strong angle dependent electronic, thermal, and optical properties. To date, some of TMTCs have been successfully synthesized and their anisotropic physical properties have been experimentally observed, which make them desirable candidates for fabrication of nanoelectronics devices with anisotropic responses[31, 32].

CHAPTER 2

NOVEL CHARACTERIZATION TECHNIQUES FOR 2D MATERIALS

2.1 Need for novel characterization techniques

This chapter will cover the characterization techniques for 2D materials. The advent of 2D materials has called for development of novel characterization techniques to study their structures and properties. As the properties of a material is highly related to its structure, understanding the structure through characterization techniques is essential in studying these novel materials. While many conventional characterization techniques are available for 2D materials, more novel techniques are necessary as the 2D materials have unique nanoscale structures compared to traditional materials, as these nanoscale structures are beyond the limits of conventional techniques. Since early 1980s, physicists have developed many new techniques such as atomic force microscope and scanning tunneling microscope, which have boosted the development of the field. Some of these novel techniques, along with a few conventional characterization techniques used for 2D materials, will be introduced in the following sections.

2.2 Characterization techniques for 2D materials

2.2.1 Raman spectroscopy

Raman spectroscopy is a fundamental characterization technique for 2D materials. The basic working principle of Raman spectroscopy is inelastic scattering: when an incident light interacts with a solid, liquid or gas molecule, the photon excites the molecule to a virtual energy state and scatters inelastically. After interaction with the photon, the molecule will be in a different vibrational or rotational state. Because of the conservation of system energy, the energy of the scattered photon will also change, which

can be probed by the change of frequency of the incident light. If the final vibrational/rotational state of the molecule is lower in energy, the scattered photon will gain energy, causing a Stokes shift. If the final state is higher in energy, scattered photon loses energy and causes an anti-Stokes shift. However, only vibrational/rotational state shifts that introduce a change in polarizability will exhibit a Raman effect.

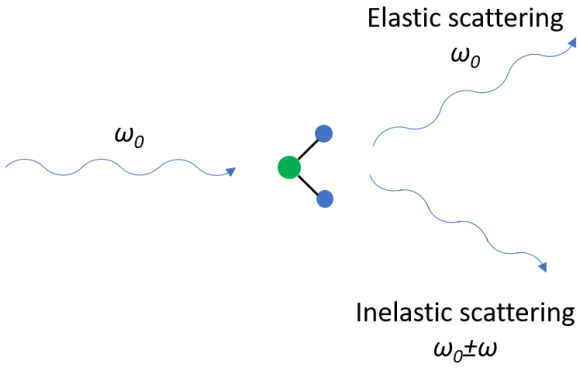

Figure 2.1 Rayleigh and Raman scattering with a single molecule

In a 2D material system, the interaction between light and the material also occurs through polarizability of valence electrons. Like the atoms in a single molecule, atoms in the lattice of a 2D material also vibrate near their equilibrium position. However, the vibration modes of atoms in lattice can't be simply visualized as in the case of a single molecule which has very limited number of atoms. After solving their equations of motions, the solutions are found to be in plane wave forms with a uniform frequency. These wave form solutions describe the lattice vibration, which can be viewed as quasiparticles named phonons. Similar to a single molecule, the arrangement of atoms in a lattice determines the phonon modes available. The lattice vibration causes the susceptibility of the lattice to oscillate in the same frequency (ω_l). When an incident light interacts with the lattice, its electric field (with a frequency of ω_0) induces a polarization

through the susceptibility. Therefore, the resulting polarization will have components modulated by the lattice vibration. These modulated components lead to Raman side bands in the scattered light. Following is a mathematical derivation of the modulation of polarization induced by lattice vibration.

Polarization $\boldsymbol{P}$ induced by the electric field $\boldsymbol{\xi}_0$ of incident light is:

$$\boldsymbol{P} = \boldsymbol{\varepsilon_0 \chi \xi_0}$$

where $\boldsymbol{\chi}$ is the susceptibility of the material. As discussed above, $\boldsymbol{\chi}$ is oscillating with the lattice vibration (with a frequency of ω_l) and it is a function of atomic coordination (X) in lattice which can be approximated as follows:

$$\boldsymbol{\chi} = \boldsymbol{\chi}^0 + \left(\frac{\partial \boldsymbol{\chi}}{\partial X}\right) X$$

As the solution of lattice vibration is in the form of plane waves, the atomic coordination can be approximated as $X = X_0 \cos(\omega_l t)$. Meanwhile, the electric field of the incident light can be described as $\xi_0 = \widehat{\xi_0} \cos(\omega_0 t)$, the resulting polarization is then expressed as:

$$\boldsymbol{P} = \boldsymbol{\varepsilon_0 \chi^0 \widehat{\xi_0}} \cos(\omega_0 t) + \boldsymbol{\varepsilon_0} \frac{\partial \boldsymbol{\chi}}{\partial X} X_0 \widehat{\boldsymbol{\xi_0}} \cos(\omega_l t) \cos(\omega_0 t)$$

$$= \boldsymbol{\varepsilon_0 \chi^0 \widehat{\xi_0}} \cos(\omega_0 t) + \frac{1}{2} \boldsymbol{\varepsilon_0} \frac{\partial \boldsymbol{\chi}}{\partial X} X_0 \widehat{\boldsymbol{\xi_0}} [\cos(\omega_0 + \omega_l) t + \cos(\omega_0 - \omega_l) t]$$

The first term in the final expression represents the elastic scattering, which has the same frequency as the incident light. The latter two terms represent inelastic scattering in which the scattered photon has a frequency of $(\omega_0 \pm \omega_l)$, also known as Raman side bands.

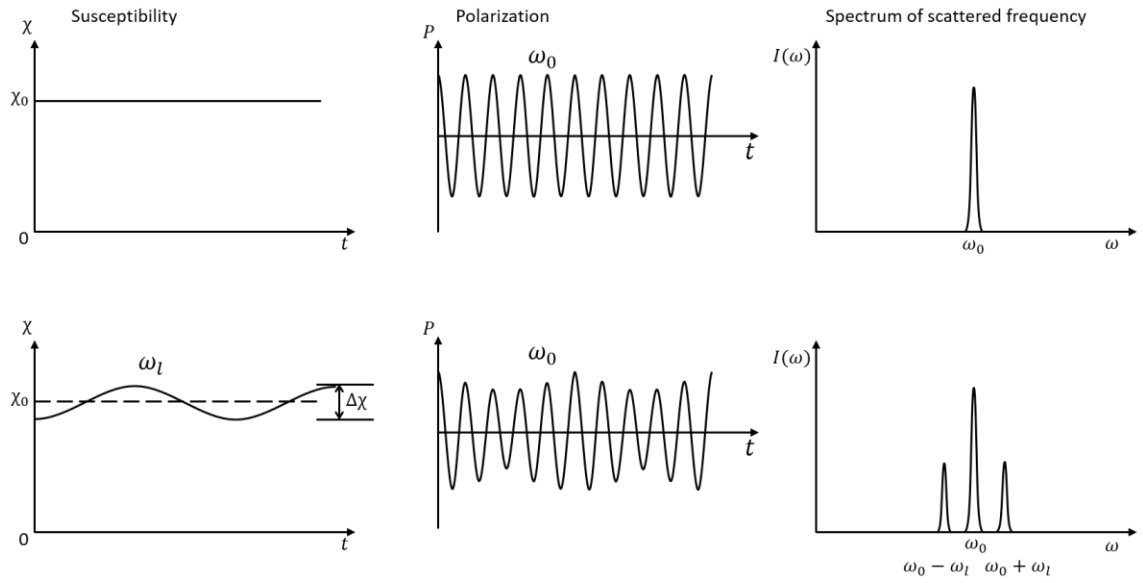

Figure 2.2 Illustration of Raman scattering

Note that the term $\partial\boldsymbol{\chi}/\partial X$ in the polarization expression above must be a non-zero term for the Raman lines to be observed. Since the atoms in a lattice are positioned in three dimensions, the susceptibility is therefore expressed in the form of a tensor. The crystal symmetry determines the symmetry properties of the susceptibility tensor. Other than the lattice structure, geometry of experiment (how the polarization of laser and detector are aligned with respect to the sample orientation) also determines whether a certain phonon mode can be observed. To demonstrate this, we will use the Raman spectra of Bi_2Se_3 recorded under different experiment setups as an example. Bi_2Se_3 has a trigonal structure, with a C_3 axis along the *c* axis of the unit cell. Its structure is highly symmetric; therefore, its normal susceptibility tensor has the following form:

$$\boldsymbol{\chi}^0 = \begin{bmatrix} \chi_{xx}^0 & 0 & 0 \\ 0 & \chi_{yy}^0 & 0 \\ 0 & 0 & \chi_{zz}^0 \end{bmatrix}$$

When an incident light from z direction (along c axis of unit cell) with its polarization along x direction is applied to the material, three phonon bands (two A_g bands and one E_g band) can be observed with a polarization also in the x direction (-ZXXZ configuration), but only one phonon band (E_g band) can be observed with a polarization in the y direction (-ZXYZ configuration). For the two A_g phonon bands, the corresponding lattice vibration are both along the c axis of the unit cell so they don't break the symmetry of the lattice along x and y directions. Therefore, the change of susceptibility tensor will be in the same format as the normal susceptibility tensor, which means that the $\partial \boldsymbol{\chi}_{xy}/\partial X$ element in the tensor will still be zero. However, for the E_g phonon the vibration mode is along the y direction and breaks the lattice symmetry, which introduces a non-zero $\partial \boldsymbol{\chi}_{xy}/\partial X$ element in the susceptibility tensor. For the above reasons, the E_g phonon band can be observed under both -ZXXZ and -ZXYZ configurations, whereas the two A_g phonon bands can only be observed under -ZXXZ configuration.

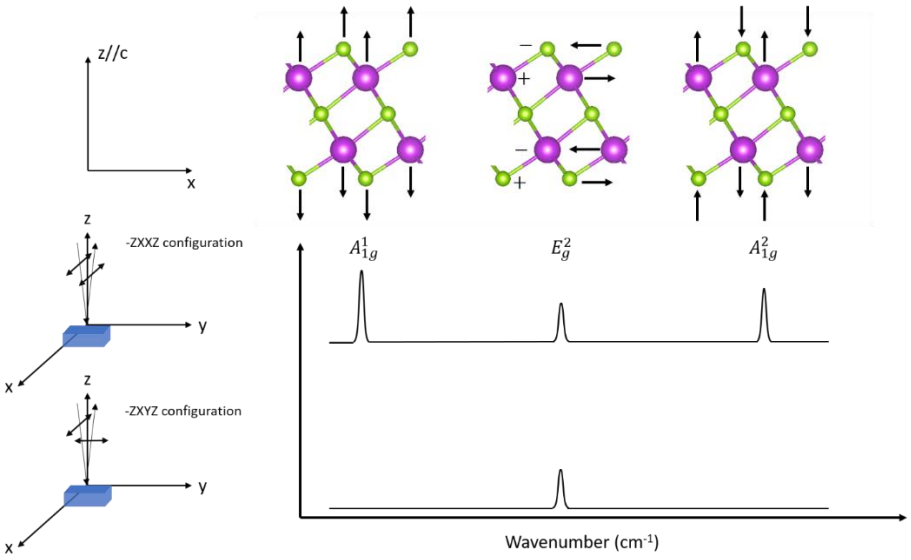

Figure 2.3 Raman spectra of Bi_2Se_3 recorded with different experimental setups

The example above also applies to 2D materials[33, 34]. In some materials, there exist phonon modes that are along a certain crystal direction that introduces a non-zero component element in the susceptibility tensor in that direction but the susceptibility change in the perpendicular direction is zero. When this material is probed with a backscattering configuration in which the polarization of incident light is perpendicular to the direction of the phonon mode, that phonon mode will not be observed. However, if the sample is rotated in the lateral direction so that the angle θ between the light polarization and phonon mode direction is less than 90^o, one starts to probe the phonon band, whose Raman intensity scales linearly with $\cos^2\theta$. This is particularly useful for studying materials with low crystal symmetry where a lot of phonon bands introduce susceptibility change along one axis of the unit cell: by plotting the Raman intensity of a certain phonon band against the angle, the orientation of lattice structure of the sample can be determined[27, 31, 33, 35].

Other than the application above, Raman spectroscopy can also be used to determine the thickness of a 2D material. A good example to demonstrate this is $MoTe_2$. In monolayer form, $MoTe_2$ has two Raman active phonon bands (E' and A_1'). However, in bilayer $MoTe_2$, the interlayer vibration gives rise to one more Raman active band A_{1g}. The intensity of this A_{1g} band is maximized at two layers, and then decreases with the increase of layers. In bulk $MoTe_2$, this vibration mode is Raman inactive. The reason for the Raman inactive to active transition with the decrease of thickness has been proposed to relate with translational symmetry breaking along the c-axis in few layer $MoTe_2$[36].

When probing 2D materials with Raman spectroscopy, the defects in the material can highly impact the results. As the Raman scattering is based on lattice vibration,

defects in the crystal affect the lattice vibration, resulting in widening of Raman peaks from the material or even additional features in the Raman spectrum[37, 38]. With the increase of defect concentration, the peak width increases. For this reason, Raman spectroscopy can be used to determine the crystallinity of a material.

2.2.2 Photoluminescence spectroscopy

Luminescence refers to the radiative emission process in solid materials. Photoluminescence, in particular, refers to light emission after absorbing a higher energy photon. Photoluminescence spectroscopy is capable of studying the emission mechanism in materials, which is necessary for developing luminescent devices such as light-emitting diodes (LEDs) and lasers. Because the emission mechanism in a semiconductor is determined by its electronic band structure, the following paragraphs will cover the basics of band theory in semiconductors to gain a good understanding of photoluminescence spectroscopy.

Quantum theory predicts that the energy states in an isolated atom have discrete energy levels. In the case of a solid material, the atoms are packed in a way that their outer orbitals start to overlap and interact with each other. According to Pauli exclusion principle, no two electrons are allowed to have the same set of quantum numbers. Therefore, the atomic orbitals in each atom split into more molecular orbitals with discrete energy levels. Since the number of atoms in a solid material is so large ($\sim 10^{21}$), the number of molecular orbitals is very large, the energy difference between adjacent molecular orbitals is so small that they can be considered as an energy band.

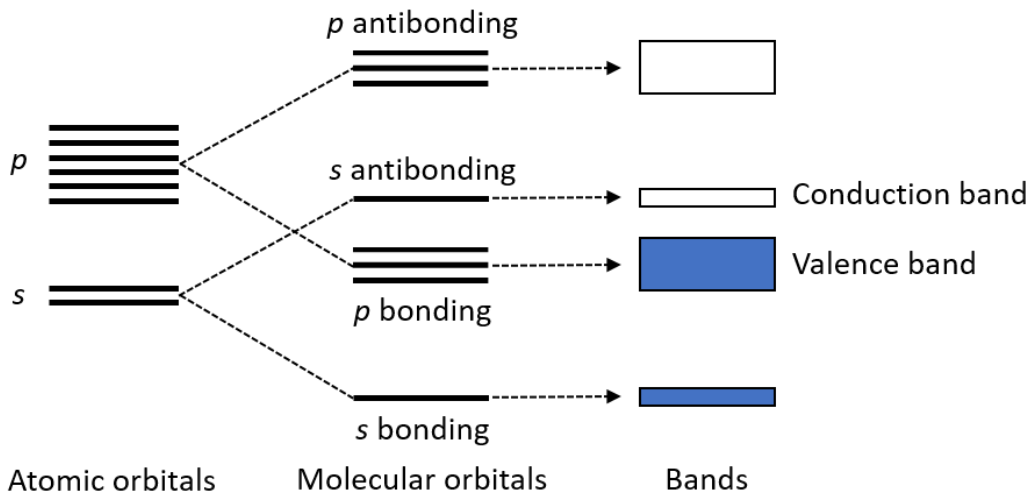

Figure 2.4 Formation of bands in solids.

In the case of semiconductors and insulators, the highest occupied band is occupied by the valence electrons from the atoms, and therefore it is named valence band. The bands that are higher in energy than the valence band are empty, and are named conduction bands. The energy difference between the top of the valence band and the bottom of the conduction band is defined as the fundamental bandgap of a semiconductor. The energy maxima state of the valence band (VBM) and energy minima state of the conduction band (CBM) have their corresponding momentum. If the momentum of the valence band maximum and conduction band minimum are same, the corresponding band gap is defined as a direct band gap, otherwise it is defined as an indirect band gap. These two types of band gaps are very important in the interband absorption and emission in semiconductors, which will be discussed in the following section.

When an electron absorbs energy from a photon, it jumps from a lower energy band to a higher energy band. This electronic transition can only happen if an electron

exists in the initial state in the lower energy band, and the final state in the higher energy band is empty, which can be easily fulfilled in semiconductors because of the presence of the valence and conduction bands. When an electron from the valence band is excited to the conduction band, its initial state in the valence band will be left as unoccupied. This process is equivalent to creating a hole in the valence band and an electron in the conduction band, therefore this interband absorption process can be considered as the creation of an electron-hole pair (e-h pair). The excited electron in the conduction band can then relax to the lowest energy state within the band through interaction with phonons, which results in electrons accumulating at the bottom of the conduction band. Similarly, holes created in the valence band also relax to their corresponding lowest energy state at the top of valence band. When this excited electron in the conduction band drops to the valence band through the emission of a photon, interband luminescence occurs, which is also known as radiative recombination of an electron-hole pair. In direct gap semiconductors, the momentum at CBM and VBM are same, therefore the corresponding electron transition is possible with the emission of a photon alone. However, in indirect gap semiconductors, momentum at CBM and VBM are different, which means that the momentum of electron must change for the corresponding transition to be allowed. This requires that a phonon must be emitted or absorbed for the conservation of momentum in radiative recombination process in indirect gap semiconductors. Because of this, the process involves emitting both a photon and a phonon, making it a second-order process. The corresponding transition probability is relatively small compared to transition in direct gap semiconductors, resulting in low luminescence efficiency. For this reason, indirect gap semiconductors are generally bad

light emitters. Two of the most important semiconductors, namely silicon and germanium, are indirect gap semiconductors and therefore generally not used as light emitters.

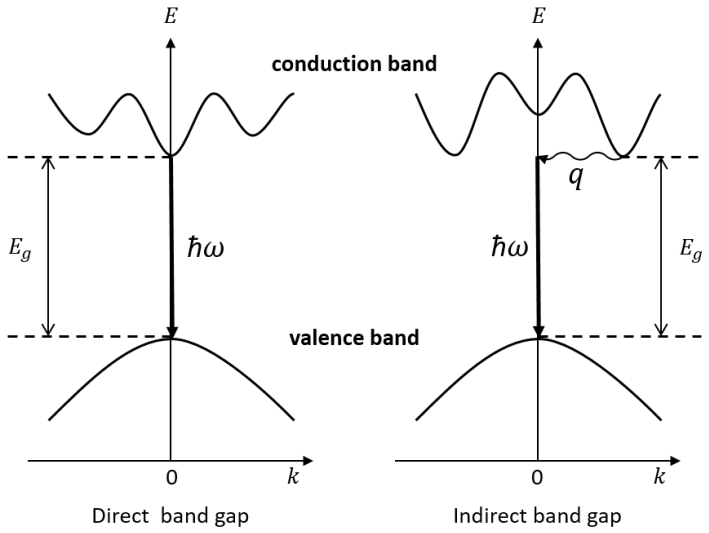

Figure 2.5 Interband transition in direct band gap and indirect band gap materials.

One assumption of the simplified discussion above on interband transition is that the interaction between free carriers (electron, hole) is neglectable. In reality, the electron and hole can interact through Coulomb force between them, which can form a bound electron-hole pair named exciton. There are two basic types of excitons: Wannier-Mott excitons, also named free excitons, and Frenkel excitons, also named tightly bound excitons. In the free exciton, the distance between the electron and hole is much larger than spacing between atoms, therefore the two particles can be considered to be moving in a uniform dielectric constant medium. This system can be approximated as a small hydrogen atom system in which the electron and hole are in a stable orbit around each other. The energy of this system can be determined by applying the Bohr model to the

exciton: the exciton has discrete energy states characterized with the principal quantum number *n*, and the energy of the *n*th state is given by:

$$E(n) = -\frac{\mu}{m_0}\frac{1}{\epsilon_r^2}\frac{R_H}{n^2}$$

where μ is the reduced mass, m_0 is the electron mass, ϵ_r is the dielectric constant of the material, and R_H is the Rydberg constant of the hydrogen atom. These exciton states are located below the CBM or above the VBM, and the energy difference between these states and corresponding CBM/VBM is the binding energy $E(n)$. Typically, the binding energy of free exciton in semiconductors is in the order of 10 meV, which is relatively small compared to the band gap (~0.5-3 eV). However, in the case of 2D materials, the thickness of the material is down to a few nanometers, which results in stronger Coulomb interactions compared to conventional semiconductors. Because of this, the exciton binding energy in 2D materials is larger, usually in the order of 0.1 eV[39, 40].

Considering the formation of excitons, actual photoluminescence in direct gap 2D materials can be depicted as follows. After absorbing a photon, an electron in the valence band is excited to the conduction band while the hole is created in the valence band. The electron and hole then interact with phonons so that they relax to CBM/VBM. This electron can undergo radiative emission before forming an exciton, and this radiative recombination process is named free carrier recombination. The energy of a photon emitted from this process is equal to the band gap (also known as electronic band gap). If the exciton is formed, the electron will first relax to the exciton energy level below the CBM and then undergo radiative recombination. In this case, the energy of the emitted

photon will be $E_g - E(n)$, and this energy difference between the exciton energy level and VBM is also known as optical band gap.

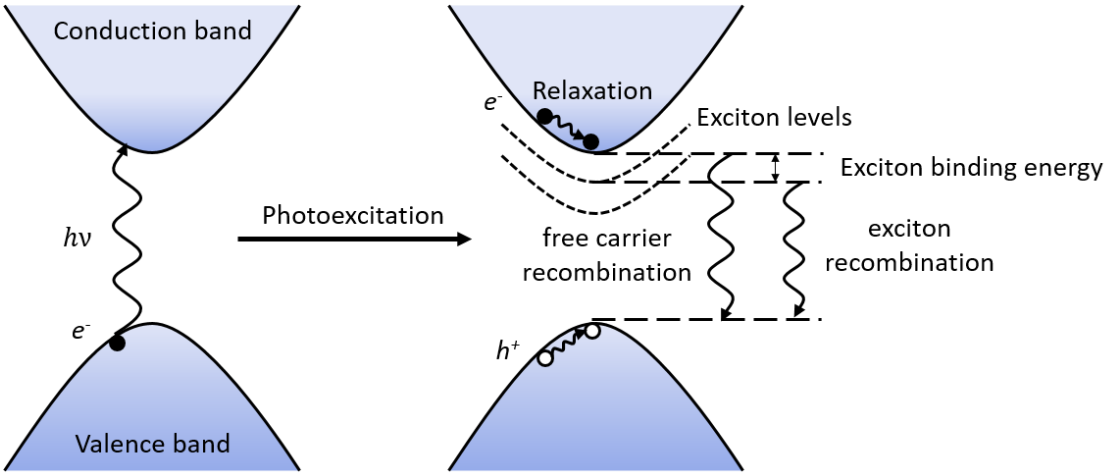

Figure 2.6 Schematics of photoluminescence in semiconductors

Other than radiative recombination, the excited electron in the conduction band can also lose its energy through many other processes, including non-radiative relaxation, and Auger recombination. In non-radiative relaxation, an electron can lose its energy through interaction with phonons, or through energy transfer to defects. In Auger recombination, the energy of the electron is given to a third carrier which is excited to a higher energy level. This carrier then loses its energy through phonon interaction[41]. When the non-radiative recombination process occurs in a shorter time scale compared to radiative recombination, overall luminescence from the material will be very low.

The basic experimental setup of photoluminescence spectroscopy consists of a light source (usually laser), a microscope system with filter, a spectrometer, and a CCD detector. In the resulting PL spectrum, PL intensity (counts of photons with a certain energy captured by the detector) is plotted against photon energy. The first piece of information that can be obtained from a PL spectrum is the optical band gap of the

material, which is found at the peak position in the spectrum. If the PL spectrum is recorded at a low temperature, the excitonic features can be observed as well. For example, at liquid nitrogen temperature (77 K), free carrier recombination peak and exciton recombination peak can be observed simultaneously as two individual peaks where the difference between their peak positions is the exciton binding energy. In summary, photoluminescence spectroscopy is a reliable, reproducible, non-contact method to study the emission mechanism in 2D materials.

2.2.3 Atomic Force Microscopy

Atomic force microscopy (AFM) is one type of scanning probe microscopy (SPM) developed in the early 1980s which has a resolution on the nanometer scale. The high spatial resolution of AFM enables scientists to visualize nanoscale structures which is otherwise extremely difficult. For this reason, the advent of AFM and other SPM techniques boosted the research of nanomaterials. For the study of 2D materials, AFM is mainly used for imaging of surface topography and investigating mechanical properties.

The basic working principle of AFM is probing the force between the sharp tip fixed on a cantilever and the sample surface[42, 43]. When the cantilever is in close proximity of the sample surface, the force (Van der Waals, electric, magnetic, etc.) deflects the cantilever and its movement is recorded by the detector. For imaging purpose, there are a few operation modes for AFM. In the contact mode, the tip on cantilever is in contact with sample surface and dragged through. However, the contact mode applies a strong lateral force onto the surface and could cause sample damage or removal of objects that are loosely attached. To overcome this issue, AFM can operate in tapping mode where the cantilever is slightly lifted from sample surface and made to

oscillate at or near its resonance frequency with a constant amplitude and frequency. When the tip is close the sample surface, the interaction between the tip and surface changes the oscillation amplitude of the cantilever. This change in oscillation amplitude is then used as a parameter to adjust the height of cantilever above the sample to keep it constant while the tip scans over the sample. In this way, damage introduced on sample surface during measurement is minimized, enabling the tapping mode to be a reliable method to compare the surface topography of a same sample before/after a certain process.

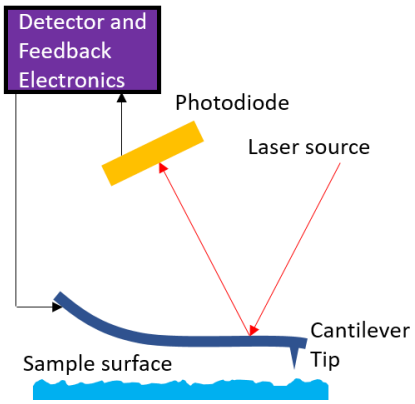

Figure 2.7 Schematics of an atomic force microscope

Other than surface imaging, the AFM system is capable of many other measurements with small adjustment on the equipment. For instance, conductive AFM (cAFM) measures the topography and electric flow at the tip position simultaneously[43]. Compared to normal AFM equipment, cAFM also requires a conductive tip, a voltage source which can be applied between the tip and sample holder, and a preamplifier that analogical current signal into digital voltages for computer. During operation, the applied voltage can be set at a constant value while the tip moves over the surface to map the current response, or the tip can be fixed at a certain position on the surface and the

voltage is varied to obtain the I/V curve on that location. cAFM is extremely useful in studying the electric properties of 2D materials because it probes the material at nanometer scale resolution.

Another variant of AFM is the Kelvin probe force microscopy (KPFM), also known as surface potential microscopy. In KPFM, work function, defined as the minimum amount of energy required to remove an electron from a material to vacuum level, of a material surface can be measured on the surface at the resolution of an AFM measurement[43, 44]. In reality, the work function of a material is highly affected by its surface, such as adsorbed molecules on the surface.

The working principle of KPFM is based on the measurement of electrostatic force between the AFM tip and sample. The tip in KPFM measurement is applied with a voltage composed of a DC and an AC component at frequency ω. When the tip and sample are brought to contact, both bias voltage and the difference between work functions of the tip and sample (also known as contact potential difference or CPD) contribute to the total voltage difference:

$$V_{total} = V_{DC} + V_{AC}\sin\omega t - V_{CPD}$$

where V_{DC} is DC bias voltage, V_{AC} is AC bias voltage. Total electrostatic force between tip and sample can be written as:

$$F = \frac{1}{2}\frac{dC}{dz}V_{total}^2$$

in which C is the capacitance, z is the distance between tip and sample. Applying V_{total} into the equation above:

$$F = \frac{dC}{dz}[\frac{1}{2}(V_{DC} - V_{CPD})^2 + (V_{DC} - V_{CPD})V_{AC}sin\omega t + \frac{1}{4}V_{AC}^2(1 - cos2\omega t)]$$

In this expression, the second term $(V_{DC} - V_{CPD})V_{AC}sin\omega t$ is related to both $(V_{DC} - V_{CPD})$ and ω, which can be utilized to determine the contact potential difference: the oscillation of cantilever at frequency ω is tracked during measurement while V_{DC} is adjusted. If the oscillation response at frequency ω becomes zero, the term $(V_{DC} - V_{CPD})V_{AC}sin\omega t$ must be zero, therefore V_{DC} applied to the tip must be equal to V_{CPD}. Since V_{CPD} is the work function difference between the tip and sample, the work function of the tip can be calibrated with a sample with known work function and then used for the work function measurement of an unknown sample.

CHAPTER 3

SYNTHESIS OF NOVEL 2D MATERIALS

There are two major methods for the synthesis of 2D materials: isolation of monolayer materials from bulk crystals, and chemical/physical vapor deposition techniques. The first method is based on the weak interlayer interaction of bulk layered crystals, and usually yields high crystallinity samples. However, the dimension of samples created by this method is very limited and therefore is not practical for large scale production. Vapor deposition technique, on the other hand, yields large area samples with relatively low crystal quality. The details of these two methods will be covered in this chapter.

3.1 Isolation of monolayers from bulk crystals

3.1.1 Mechanical exfoliation

There are two major methods to thin down a bulk layered material: mechanical exfoliation and chemical exfoliation[3, 45]. The most common method for isolating monolayers from bulk crystals is mechanical exfoliation. This is usually achieved by placing a piece of crystal between adhesive tape and cleaving repeatedly. Because the Van der Waals interaction between layers is very weak, it can be effectively broken by exfoliation, thinning down the material. The resulting tape is then pressed against a target substrate and peeled off, leaving some thin samples on the substrate.

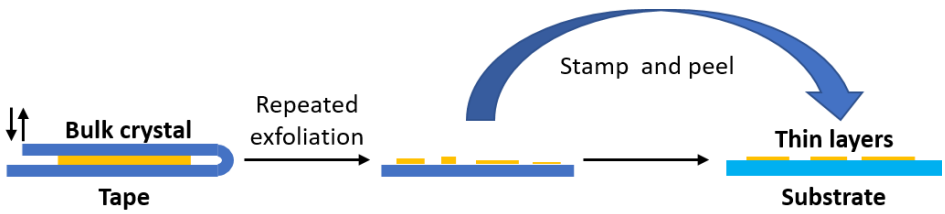

Figure 3.1 Schematics of mechanical exfoliation with tape

3.1.2 Bulk crystal growth

The growth of layered bulk crystals is a more complex process compared to mechanical exfoliation. Although the bulk crystal for some materials are readily available in nature, such as graphite and molybdenite, most of them must be synthesized in laboratories. Chemical vapor transport (CVT), which has been traditionally used for purification of metals and growth of highly crystalline compounds[46], is the major approach adopted by material scientists to grow high quality bulk crystals of layered materials. For the synthesis of a binary compound, it involves the vaporization of the two pure elementals in a temperature gradient. The vaporized elementals will react and the formed compound will be transported by the temperature gradient and crystallize somewhere else in the system. According to the Le Chatelier's principle, if the reaction that forms the desired compound is exothermic, the transport of the materials will be from high temperature to low temperature.

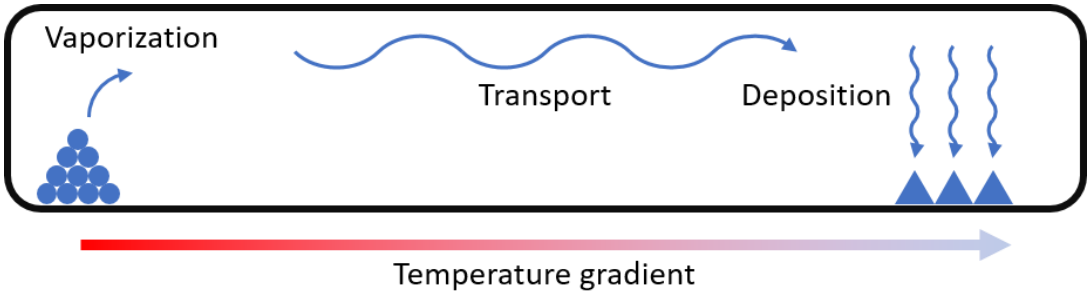

Figure 3.2 Schematics of chemical vapor transport.

Pratically, CVT is performed in a sealed ampoule containing the two elemental reactants. The ampoule is then placed in a two-zone furnace where the temperature of the two zones can be set independently to achieve a temperature gradient. In order to obtain high crystallinity, the entire process is slowed down to achieve thermodynamic

equilibrium: ampoule is slowly heated up (ramp rate is usually below 1°C/min) to the desired temperature and then the system is maintained for several days followed by controlled cooldown (also below 1°C/min)[31, 32, 47].

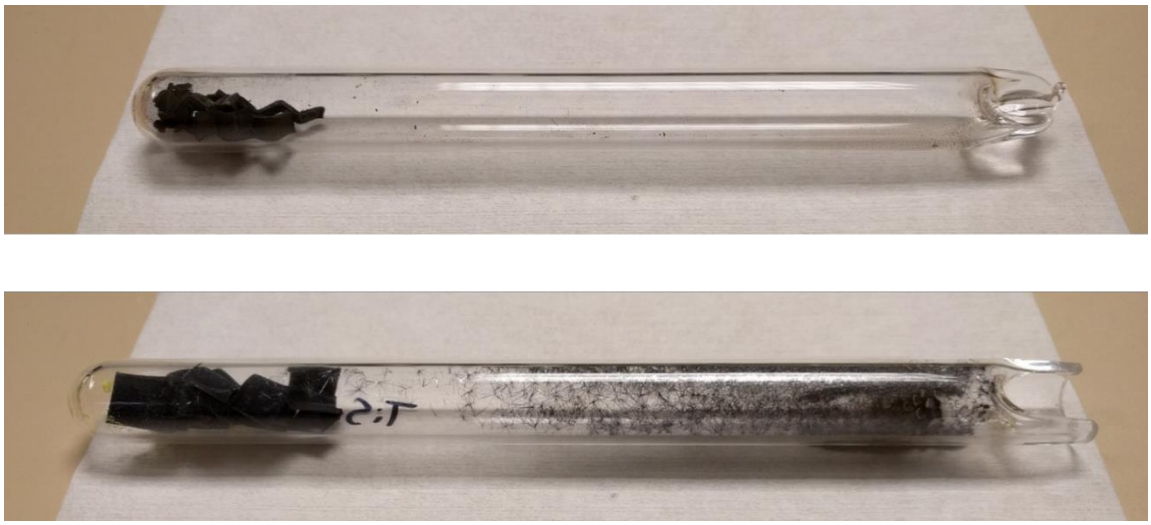

Figure 3.3 Examples of CVT ampoules before (top) and after (bottom) growth.

3.2 Chemical/Physical vapor deposition techniques

Vapor deposition is the major technique to directly grow ultrathin layered material on a substrate[9, 16, 27, 48, 49]. Depending on whether there is a chemical reaction required to form the desired material or not, the process can be categorized in chemical/physical vapor deposition (CVD/PVD). Despite this difference, the working principle of these two processes are same. Overall, CVD/PVD process consists of many steps that can be categorized into the following two: mass transport and surface reaction. Generally, vapor deposition process utilizes a tube furnace with a quartz tube chamber. Precursor materials are heated and vaporized and then transported by a carrier gas (usually an inert gas such as nitrogen or argon) to another zone in the furnace where the target substrate for growth is placed. The precursor materials then diffuse onto the surface

of the substrate and growth is achieved. In CVD process, the precursor materials undergo a chemical reaction on the surface of substrate and the compound formed crystallizes, whereas in PVD process the precursor material directly crystallizes on substrate.

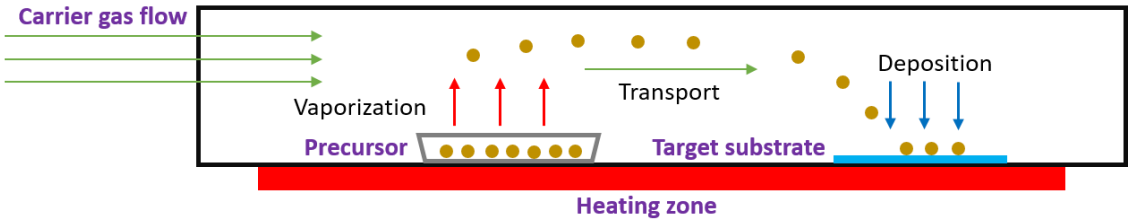

Figure 3.4 Schematic of vapor deposition process.

The outcome of vapor deposition is very sensitive to many experimental parameters because of the physical/chemical processes involved. A few of these parameters include temperature profile (which includes temperature and ramp rate), growth time, flow rate of the carrier gas, distance between precursor material and target substrate. To understand the effects of parameters, we need to review the processes mentioned above in detail. Since the two major steps are mass transport and surface reaction, the one that is slower will determine the overall growth rate. According to the Arrhenius equation, the rate of reaction increases exponentially with the increase of temperature. As a result, at low temperature, the rate limiting step is surface reaction, whereas at high temperature the rate limiting step is mass transport.

When the process is mass transport limited, the diffusion of precursor molecules from the mass flow to the substrate is a typical rate limiting step. The carrier gas flow rate is usually small in vapor deposition, which results in laminar flow of the gas within the tube. In a laminar flow system, fluid flows in parallel layers without lateral mixing, which means that there is no mass exchange between layers and diffusion is the only way

for precursor gas molecules to travel between different layers. When the gas enters the tube or hits the wafer substrate, because of its viscous nature, the flow speed at the boundary is zero and increases to the mass flow speed along the cross-sectional direction. In fact, the local flow speed of a certain point in the system is related to both x and y coordinate when we form a Cartesian coordinate from the side view.

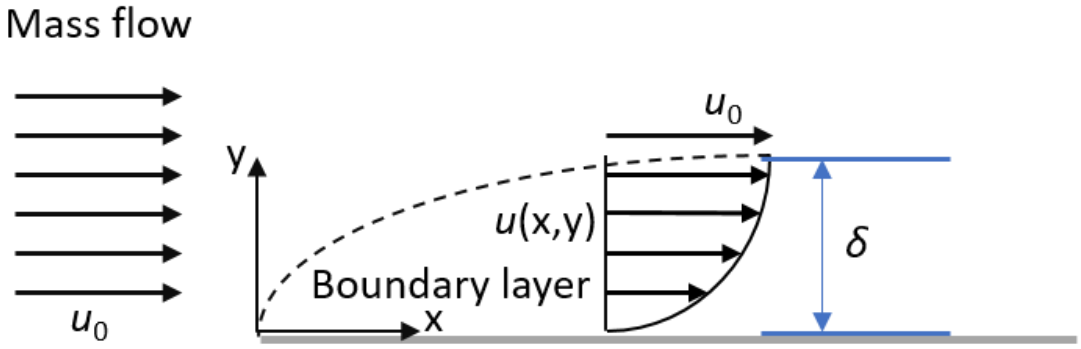

Figure 3.5 Schematic of boundary layer in a laminar flow system

In the figure, the area near the boundary with a flow speed lower than 99% of the mass flow speed is considered as the boundary layer. As the flow speed at the boundary is zero, the precursor molecule concentration is also zero. Therefore, the molecules must diffuse through the boundary layer by diffusion. The profile of the boundary layer thickness δ is given by:

$$\delta \approx \sqrt{\frac{\nu x}{u_0}}$$

where $\nu = \mu/\rho$ is the kinematic viscosity (μ is the dynamic viscosity and ρ is the density), x is the distance, and u_0 is the mass flow rate. Assuming the temperature is constant and the carrier gas type is not changed, the boundary layer thickness increases with the distance and decreases with mass flow rate.

According to Fick's law, the diffusion flux of molecules (J) can be written as:

$$J = -\frac{D}{RT}\frac{dc}{dy}$$

where D is the diffusivity of the reactants, c is the concentration, and y is the radial distance. The concentration gradient part can be approximated as:

$$\frac{dc}{dy} \approx \frac{\Delta c}{\Delta y} = \frac{c_b - c_s}{\delta}$$

c_b is the concentration in mass flow and c_s is the concentration at the surface, which is effectively zero. From here we can see that when the boundary layer thickness is high, the diffusion flux is small, and the amount of precursor molecules that can reach the substrate will be small.

After diffusion through the boundary layer, the molecules deposit onto the substrate through nucleation and growth. Thermodynamics of a gas molecule nucleating onto a surface can be described with the Terrace Ledge Kink (TLK) model: when an adatom forms on the substrate surface by adsorption, this adatom will diffuse into an existing terrace or kink site on the surface, where its energy will be minimized. The nucleation rate is governed by the ratio between the mean free path for diffusion of an adatom on the surface $\bar{x}$ and the ledge spacing λ. If $\lambda >> \bar{x}$, most adatoms will not be able to diffuse to the terraces or kink sites and will desorb instead. When $\bar{x} >> \lambda$, new adatoms on the surface can easily approach the terraces or kink sites and the nucleation rate will be high. After nucleation, there are three basic growth modes: Voller-Weber, also named island mode, depicts the growth where small stable clusters form after nucleation and continue to grow in three dimensions. In this growth mode, the interaction between the deposit molecules is strong so they tend to bind to each other than to the substrate. The

second growth mode is Frank-van-der Merwe mode, in which the deposit molecules bind stronger to the substrate compared to each other. This mode is also named layer-by-layer growth, indicating that the growth on the lateral direction is favored over the vertical direction, which is ideal for the growth of layered materials. The third growth mode is an intermediate mode named Stranski-Krastanov mode. Initially the growth is layer-by-layer, followed by island growth.

3.2.1 MoS_2 growth

The growth of MoS_2 has been well established and is a good example to demonstrate the process of vapor deposition. The precursors that can be used are MoO_3 plus elemental sulfur (CVD process) or MoS_2 powder alone (PVD process).

Before growth, the surface of target substrates (SiO_2/Si or sapphire) are treated with piranha solution or oxygen plasma etcher to remove organic or carbon residue and create a clean surface. The MoO_3 powder is weighted and evenly placed in a ceramic boat, and the cleaned substrates are placed over the top of MoO_3 powder. This ceramic boat with MoO_3 powder and substrates is then placed in the quartz tube and positioned at the center of the furnace. Sulfur powder is weighted and placed in a separate crucible and positioned at roughly 18 cm to the upstream side in the quartz tube. The tube is then closed and nitrogen carrier gas is turned on to purge the system. The system is then slowly heated to the growth temperature and then the temperature is held for a certain period of time, followed by controlled cooling down. During the heating and cooling process, the flow rate of carrier gas can be adjusted for growth control.

CHAPTER 4

UNDERSTANDING ENVIRONMENTAL STABILITY OF TE BASED 2D MATERIALS

In this chapter, we will cover the first fundamental investigation on surface reaction mechanisms and environmental stability of tellurium containing 2D anisotropic systems such as GaTe and $ZrTe_3$. Results show that GaTe degrades in air within a few days and its Raman spectrum rapidly transforms into a completely different one. The same transformed Raman spectrum is also observed for aged 2D anisotropic $ZrTe_3$, suggesting that the observed effect could be ubiquitous among other Te-based 2D systems. By environmental Raman spectroscopy measurements under different gaseous conditions and X-ray photoelectron spectroscopy (XPS) measurements, we are able to identify that a minute concentration of $H_2O(g)$ (humidity) causes strong surface chemistry changes while a high concentration of strong oxidizing molecule, O_2, in air does not have any detrimental effects on GaTe. Lastly, the effects of surface transformation on the anisotropic material response of GaTe are studied by angle-resolved Raman spectroscopy (ARS) measurements. Overall findings significantly advance the understanding of surface transformation processes, unravel the molecular interactions that are responsible for surface degradation, and investigate anisotropic to isotropic transformation.

4.1 Degradation of Te based 2D materials

Pseudo-1D materials are a new class of anisotropic 2D materials in which atoms are arranged within a 2D plane in such a way that they form chains extending along a particular lattice direction. Some examples of this unique type of materials include black

phosphorus[50, 51], ReS_2[16, 52, 53], and $ReSe_2$[54, 55] from TMDCs, TiS_3[56-58], ZrS_3[31] from TMTCs, as well as most recently discovered GaTe[25, 26, 59] from PTMCs. The presence of strong crystalline anisotropy in these pseudo-1D materials leads to direction dependent properties wherein high electronic conductivity[50, 51, 56], thermal conductivity[60], and exciton recombination[47, 61] only occur at a given lattice direction. As such, the material properties and behavior of anisotropic 2D materials bridge across 2D and 1D materials such as nanotubes, nanowires, and other systems with a high geometrical aspect ratio.

Recently, our research group and others have reported on the anisotropic atomic arrangement, optical behavior, and Raman scattering of GaTe from the PTMC family[27, 59]. However, the environmental stability under ambient and extreme conditions of this material is currently unknown, despite its attractive direction dependent properties[23]. For GaTe, this is of particular concern because a few other tellurium based 2D materials such as $MoTe_2$ and WTe_2 have been previously suspected to suffer from environmental instability[28, 62]. In fact, different Raman spectra have been attributed to monoclinic phase GaTe by different research groups[25, 27, 59, 63]. Since Raman spectroscopy is highly sensitive to surface chemistry and structural characteristics, more work is required to gain a fundamental understanding of material stability and interactions with molecular species in air.

4.2 Investigating environmental degradation of Te based 2D materials

4.2.1 Design of experiments

GaTe samples were deposited onto Si substrates coated with 285 nm thermal oxide (SiO_2/Si) using conventional mechanical exfoliation from monoclinic GaTe crystals grown using the Bridgeman technique[64]. The monoclinic phase of exfoliated

GaTe sheets was identified with Raman spectroscopy measurements. The strong structural anisotropy in this monoclinic phase can be observed from high-resolution transmission electron microscopy (HRTEM) and fast Fourier transform (FFT) images (Figure 4.1b). Furthermore, the presence of anisotropy can be evidenced by ARS measurements: it has been previously established that the two most prominent Raman peaks at 116 and 177 cm^{-1} involve atomic vibrations along the *b*-axis. Consequently, ARS results (polar plots) of these two peaks display a $\cos^2(\theta)$-like response wherein the Raman intensity is maximized/minimized when the polarization of E-field is at an angle of $0^o/90^o$ with the *b*-axis, meaning parallel/perpendicular to the crystalline anisotropy direction (Figure 4.1e-f). This allows one to determine the anisotropy direction using fast and non-destructive Raman spectroscopy.

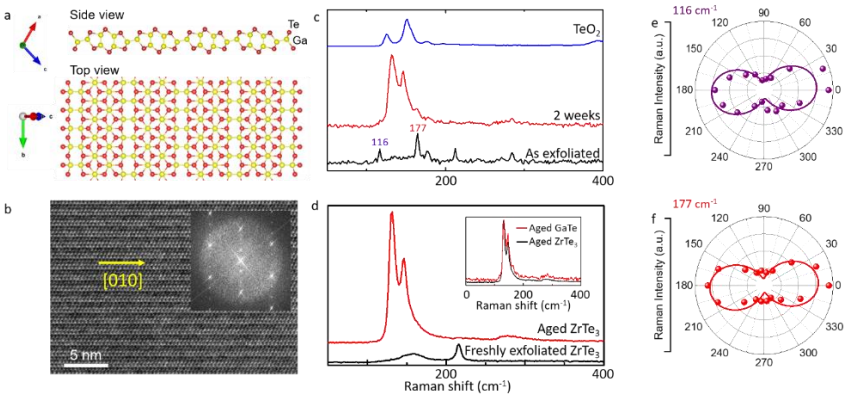

Figure 4.1 Basic characterization of monoclinic GaTe. (a) Side view and top view of a single layer of monoclinic GaTe. (b) TEM image and FFT pattern (inset) of monoclinic GaTe. (c) Raman spectra of freshly exfoliated GaTe (black line), aged GaTe (red line), and tellurium dioxide (blue line). (d) Raman spectra of freshly exfoliated $ZrTe_3$ (black line) and aged $ZrTe_3$. Inset: normalized Raman spectra of aged GaTe and aged $ZrTe_3$. (e, f) Polar plots of the Raman intensity of 116 and 177 cm^{-1} peaks of GaTe.

The Raman spectrum of exfoliated GaTe transforms quickly (within one week) into a vastly different Raman spectrum as shown in Figure 4.1c: the characteristic Raman peaks from monoclinic GaTe located at 116, 163 and 177 cm^{-1} gradually disappear, while two new Raman peaks at 126 and 142 cm^{-1} emerge and dominate the overall spectrum. Interestingly, the same Raman spectrum was observed on aged 2D anisotropic $ZrTe_3$ (Figure 4.1d). This suggests that the observed effect is not specific to GaTe but could be common among other Te-based 2D materials.

4.2.2 Interaction with gas molecules in air

To understand the origin of changes in Raman spectra with time, we have performed detailed environmental Raman spectroscopy measurements. In these experiments, freshly exfoliated GaTe flakes were stored under a certain gaseous environment to understand effects of different molecular interactions on the GaTe surface, and Raman spectra were collected before/after exposure to these conditions for one week. When the GaTe sample is kept in vacuum (<1 mTorr), the Raman spectrum remains remarkably similar to the freshly exfoliated one, suggesting that GaTe is stable in vacuum and strong Raman transformation is likely to originate from interaction with gas molecules in air (i.e., O_2, N_2, and H_2O). In fact, the effect of some residual air present in environmental chamber with a pressure above 10 mTorr can be evidenced by a small shoulder that appears in the 120-140 cm^{-1} range.

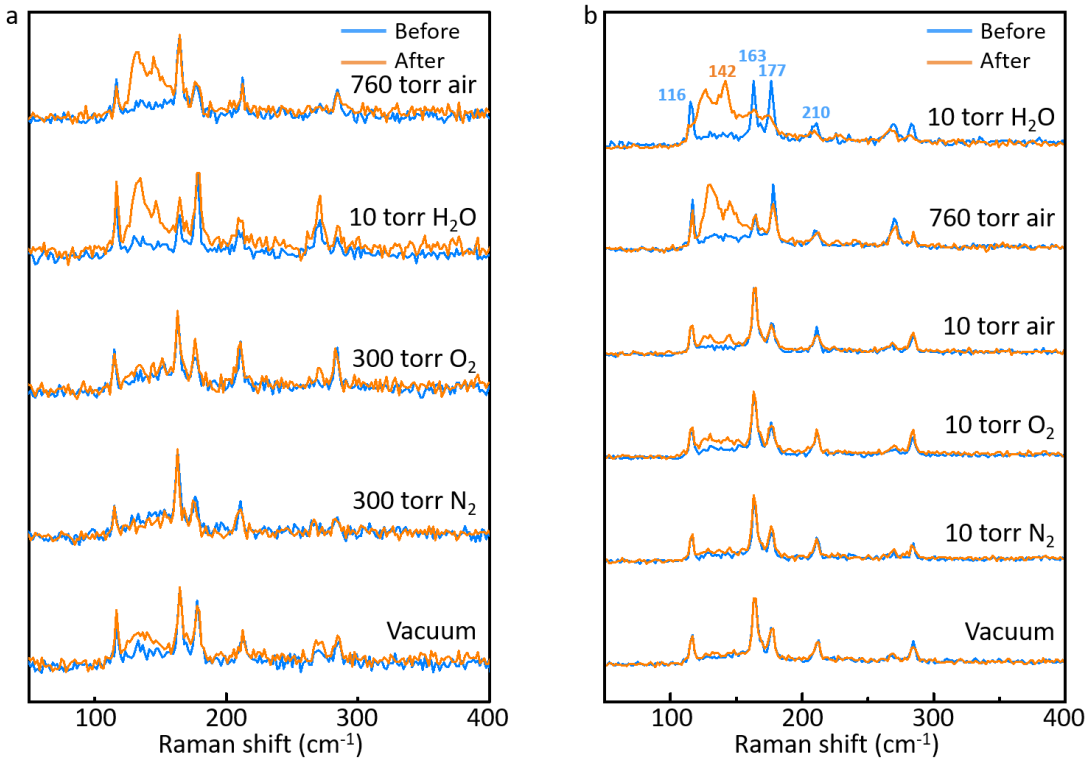

Figure 4.2 Environmental and laser induced aging of GaTe. (a) Raman spectra of GaTe before/after environmental aging in different gas environments for two weeks. (b) Raman spectra of GaTe before/after laser induced transformation in different gas environments for 15 minutes.

To determine the type of gas molecules responsible for strong surface degradation, we have performed similar measurements in air as well as under N_2, O_2, and H_2O rich environments. The samples stored in pure nitrogen or oxygen do not show any peaks at 126 or 142 cm^{-1}, but these new peaks develop immediately when samples are exposed to H_2O vapor. Based on these results (Figure 4.2a), we conclude that the observed transformation originates from interaction with H_2O molecules at the surface while N_2 and even oxidizer O_2 do not cause significant effects. Transformation of the

Raman spectra in different environments can be clearly seen in the bar graph in Figure 4.3a. In this figure, I_{142}/I_{163} in the ordinate takes the intensity ratio of the 142 cm^{-1} peak observed on aged GaTe and the 163 cm^{-1} peak that represent aged (transformed) GaTe and pristine GaTe contributions respectively. Therefore, I_{142}/I_{163} provides a measurement of degree of aging where larger I_{142}/I_{163} ratio implies more severe transformation. While I_{142}/I_{163} ratio remains mostly unchanged under vacuum, O_2, and N_2, the I_{142}/I_{163} increases dramatically by 5-10 folds when the samples are exposed to air and H_2O vapor.

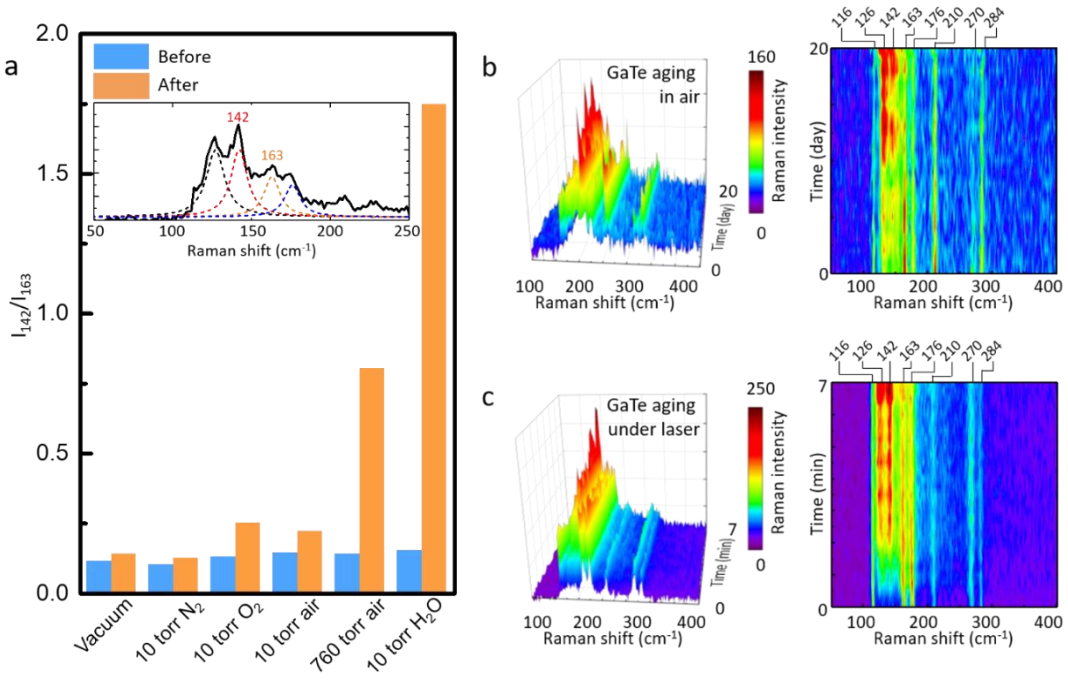

Figure 4.3 Insight of environmental and laser induced aging of GaTe. (a) Quantitative analysis of Raman spectra before/after aging. (b) 3D surface and 2D contour plot of GaTe Raman spectra evolution during aging in ambient environment. (c) 3D surface and 2D contour plot of GaTe Raman spectra evolution under laser exposure.

In addition to environmental Raman results, we have performed environmental laser induced aging effects to observe the aging process in shorter timeframes to gain

further understanding of molecular interactions at the surface. Samples were exposed to a 488 nm laser focused down to 0.75 μm^2 beam area at ~50μW power for ~10 minutes under different environments, and Raman spectra were collected immediately after exposure. Results shown in Figure 4.2b show striking similarities to Figure 4.2a which suggest laser induced aging occurs in the presence of H_2O vapor and that the aging process can be accelerated under constant laser exposure. Acceleration of the aging process can be attributed to increased chemical reaction rates by energy provided from the external laser, or by photo-active surface reaction mechanisms, and is subject to future research. Overall, the laser induced technique simply allows one to investigate environmental effects in much shorter timescales and provides a quick and effective measurement tool to assess the material's stability in different gaseous environments.

To understand the transition from pristine GaTe to aged GaTe, we have collected Raman spectra during the course of aging process in air and under laser exposure. Results convincingly show that transition from monoclinic GaTe to aged GaTe occurs gradually within a week in air or a few minutes under laser exposure without any intermediate stages of surface reaction as evidenced by the absence of other new Raman peaks and new phases of GaTe. Most notably of all, laser induced aging only occurs at regions where GaTe sheets were exposed to the laser source.

4.2.3 Anisotropic to isotropic transition

Next, we discuss how environmental aging and H_2O interaction with the GaTe surface impact overall anisotropic properties through ARS measurements. In Figure 4.4, we show polar plots of Raman peaks at 114 and 177 cm^{-1} after aging for 1 and 2 weeks. On day 0, which corresponds to freshly exfoliated GaTe sheets, intensity of the two

Raman peaks above is maximized at 180 degrees which aligns with *b* axis, meaning that the GaTe (010) direction is extending along 0-180 degrees. Similar angle resolved measurements on the same exfoliated sample show that anisotropy is gradually lost when the sample is kept under ambient conditions. This finding suggests that GaTe sheets stored under ambient conditions undergo an anisotropic (pseudo-1D) to isotropic transition as newly emerging Raman peaks (126 and 142 cm^{-1}) do not possess any anisotropic response, and better surface protection post processing methods are required to assess their true potential as pseudo-1D materials.

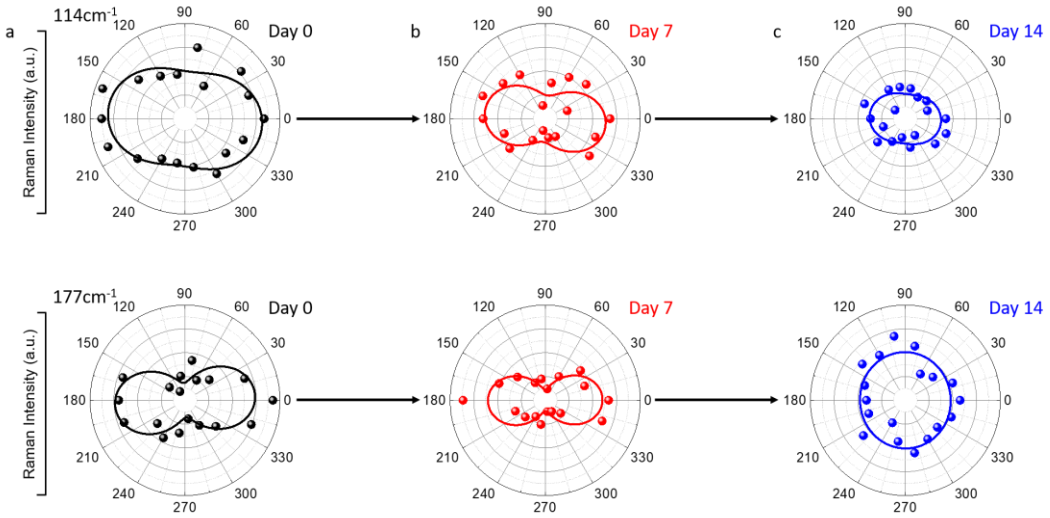

Figure 4.4 Angle resolved Raman spectra of GaTe during environmental aging. (a) Polar plots of 114 and 177 cm^{-1} peaks on day 0. (b) Polar plots of 114 and 177 cm^{-1} peaks on day 7. (c) Polar plots of 114 and 177 cm^{-1} peaks on day 14.

4.2.4 Surface morphology changes

Then the main question arises: what is the exact nature of the interaction of water molecules at the GaTe surface? To understand the fundamental mechanism behind this process, we have performed AFM, c-AFM, and XPS measurements on freshly exfoliated, environmentally aged, and laser exposed samples. AFM measurements performed on freshly exfoliated (pristine) GaTe flakes clearly demonstrate that GaTe surface quality is significantly reduced as shown in Figure 4.5. During the environmental aging process, RMS roughness of the surface increases by 50% from 0.5 nm to ~0.75 nm while the overall thickness increases by ~5 nm. This finding suggests that the interaction with H_2O is a chemical process and causes surface to change its morphology. Similar findings have also been observed for GaTe sheets aged by laser exposure under H_2O rich environment. AFM images in Figure 4.5 c-d show that laser induced aging is rather local as anticipated, and the Raman spectrum of this local spot displays the two new peaks at 126 and 142 cm^{-1} as mentioned before. Interestingly, however, laser induced aging causes these local regions to increase in height up to ~10 nm. This can be simply attributed to $GaTe \rightarrow GaTe_{1-y} + TeO_{2-x}$ partial (or full) oxidation at the surface since amorphization is known to cause material to swell in volume.

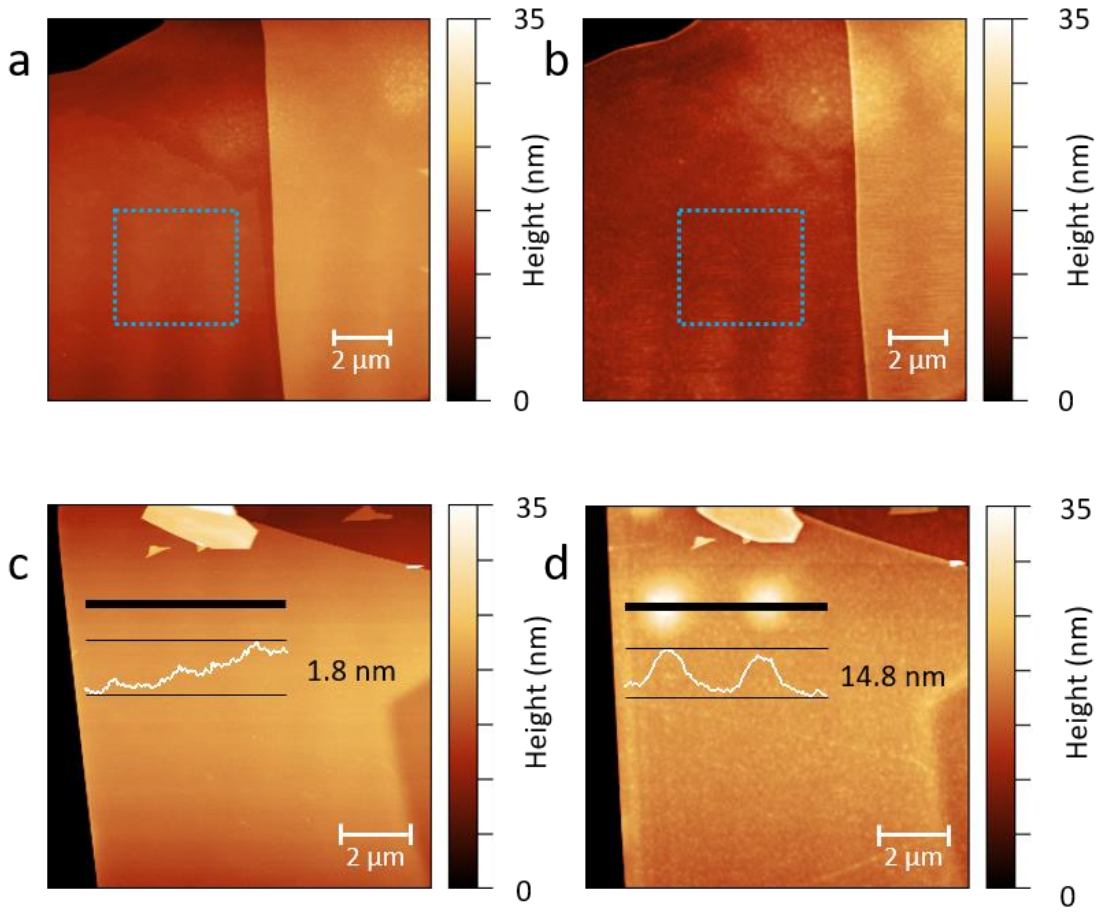

Figure 4.5 Surface degradation effects on GaTe. (a, b) AFM measurements on freshly exfoliated and environmentally aged GaTe sheets. (c, d) AFM measurements on exfoliated and laser aged GaTe sheets.

In-situ environmental XPS measurements on pristine and environmentally aged samples make this point beautifully in Figure 4.6a; tellurium peaks in pristine GaTe are originally located at 572.8 and 583.2 eV for Te $3d_{5/2}$ and Te $3d_{3/2}$ respectively which is a commonly accepted value for Te bonded in a non-oxide crystal[65, 66]. Once pristine GaTe surface is exposed to air inside the XPS chamber, new tellurium related peaks develop within a few days. These new peaks are located at 576.6 eV (Te $3d_{5/2}$) and 587.0 eV (Te $3d_{3/2}$) and closely match TeO_2 and other Te oxide complexes[65]. Here, the presence of

both non-oxide and oxidized Te peaks on the aged GaTe surface clearly suggests that some of the tellurium atoms remain bonded to gallium atoms while a substantial amount of the tellurium atoms get oxidized, likely due to strong interaction with H_2O. The effect of Te-O formation on GaTe surface also shows itself in our Schottky junction devices characterized by conductive AFM measurements (Figure 4.6b) at nanoscale. Comparison between GaTe/Pt Schottky junction characteristics measured on freshly exfoliated and aged GaTe shows that overall current density and rectification ratio decreases due to the formation of a tunnel junction like Te-O surface layer.

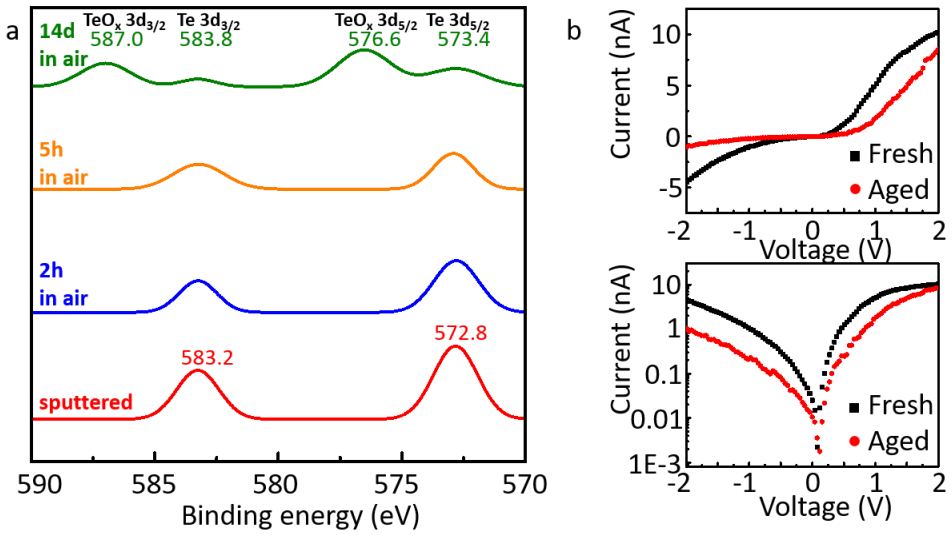

Figure 4.6 (a) Environmental XPS measurements on as-cleaved GaTe sheets. (b) *I-V* curves of as-cleaved and aged GaTe plotted on linear and semi-log scales respectively.

4.3 Summary

In summary, our results mark the very first investigation on surface reaction mechanisms and environmental stability of tellurium containing 2D anisotropic systems like GaTe and $ZrTe_3$. Our environmental studies on anisotropic Te containing nanomaterials demonstrated that freshly exfoliated GaTe layers quickly deteriorate in air. During this process, the surface morphology, Raman spectrum, structure, and surface chemistry undergo drastic changes. Our environmental XPS and Raman spectroscopy measurements suggest that H_2O gas molecules interact rather strongly on the surface while N_2, O_2, and inert gases do not have major detrimental effects on the GaTe surface. Importantly, the much desired anisotropic property of GaTe gradually disappears during aging process. Overall results establish the environmental stability of newly discovered 2D anisotropic materials GaTe and $ZrTe_3$, and offer deep insights into surface reaction process on Te-containing 2D layers.

CHAPTER 5

EXTENDING SHELF LIFE OF 2D MATERIALS

In the previous chapter we discussed the environmental instability of tellurium containing 2D materials such as anisotropic GaTe[23, 67], and $ZrTe_3$[31]. While they offer unique properties such as bandgaps in the infrared range, high structural, electrical, and optical anisotropy, the environmental instability poses difficulties in their manufacturing and applications. Previous studies have shown that interactions between air and surface can introduce anisotropic to isotropic transition[67], phase transition[68], oxidation, and intercalation[27] (Figure 5.1b). To overcome these, developing cheap, reproducible post-processing techniques to increase the environmental stability of these 2D materials without any negative effects on their physical properties is required.

In this chapter, we have adapted surface functionalization chemistry to protect tellurium based 2D materials against detrimental effects of gaseous interactions at the 2D surfaces. In particular, diazonium based surface functionalization is selected due to its success in surface grafting of graphene based 2D systems[69, 70]. Our results show that when the surface of tellurium based 2D materials is functionalized by aryl diazonium molecules, they exhibit much enhanced stability in air and even under water which is known to have negative effects. Environmental Raman spectroscopy, PL spectroscopy, atomic force microscopy, and conductive AFM measurements confirm that the surface stability is enhanced by diazonium surface functionalization without impacting its physical properties: the anisotropic response of materials is retained, bandgap stays unchanged, and light emission efficiency remains largely unchanged.

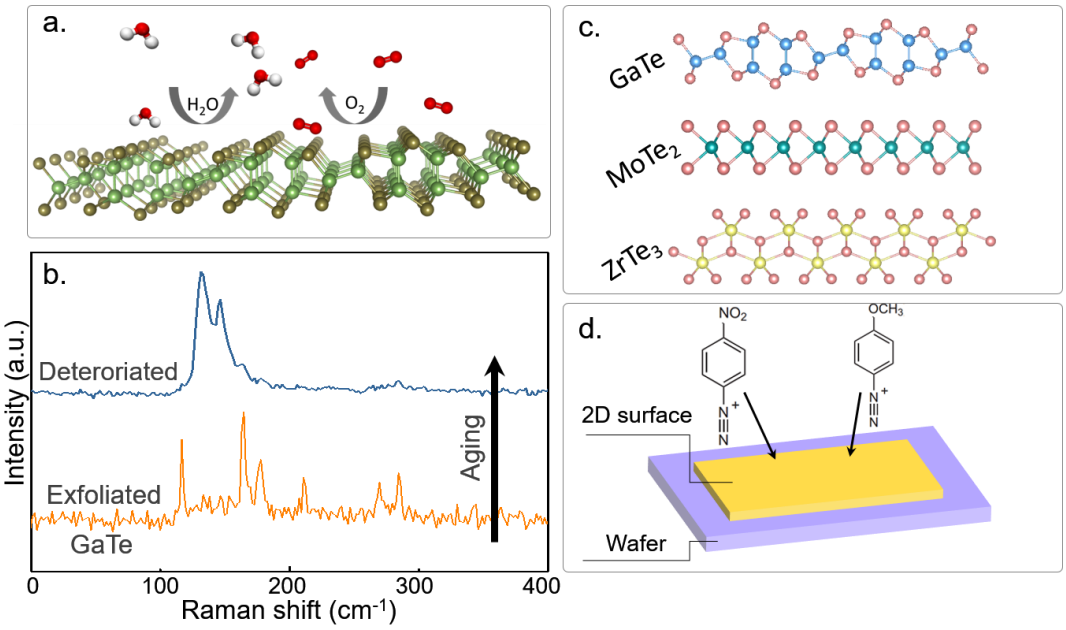

Figure 5.1 Degradation and functionalization schematics (a) Degradation scheme of tellurium based 2D materials. (b) Raman spectra acquired from exfoliated (orange line) and aged (blue line) GaTe. (c) Side view of single layer monoclinic GaTe, 2H-$MoTe_2$, and monoclinic $ZrTe_3$. (d) Molecular structures of 4-nitro/methoxy benzene diazonium salts.

5.1 General route to material stabilization

Te based 2D materials (GaTe, $ZrTe_3$, and $MoTe_2$) are exfoliated onto Si wafer with 285 nm thermal oxide (SiO_2/Si) from bulk crystals synthesized by CVT. Surface functionalization is then performed by immersing the exfoliated samples into diazonium salt solution for 15 minutes. The diazonium solution was prepared by dissolving 4-nitrobenzenediazonium tetrafluoroboride in acetonitrile with 0.1 M tetrabutylammonium hexafluorophosphate as electrolyte to make a 0.01 M solution. After this process, the sample was rinsed with acetonitrile several times to remove any residue and then dried under nitrogen flow. We noticed that the concentration of diazonium solution and

treatment time largely affects the result of functionalization. In a few attempts where the diazonium concentration was below 10 mM, surface functionalization was not successful, probably due to low surface coverage. Meanwhile, diazonium concentrations between 20 and 100 mM proved to be effective. Furthermore, we also discovered that treatment times longer than 15 minutes didn't prove to be more effective compared to 15 minutes. Therefore, the optimized surface functionalization parameters were determined to be 15 minutes of treatment in 20 mM diazonium solution.

5.2 Results of surface functionalization

5.2.1 Enhanced material stability

Prior to surface functionalization, the exfoliated Te based 2D material samples were characterized by Raman, PL spectroscopy, AFM and c-AFM to identify their material properties and surface quality. The surface functionalization process mentioned above was then applied to the samples followed by environmental aging under ambient conditions for two weeks. Our results on GaTe show that the environmental stability has been significantly enhanced in air. As shown in Figure 5.2a, the functionalized GaTe sample showed no major change in its Raman spectrum after two weeks of aging in air. When we extended the aging time to four weeks, only minimum Raman change was observed as well. This result is highly consistent over more than 50 different samples with varying thickness. Meanwhile, $ZrTe_3$ and $MoTe_2$ samples processed by surface functionalization also showed enhanced environmental stability as shown in Figure 5.2b-e.

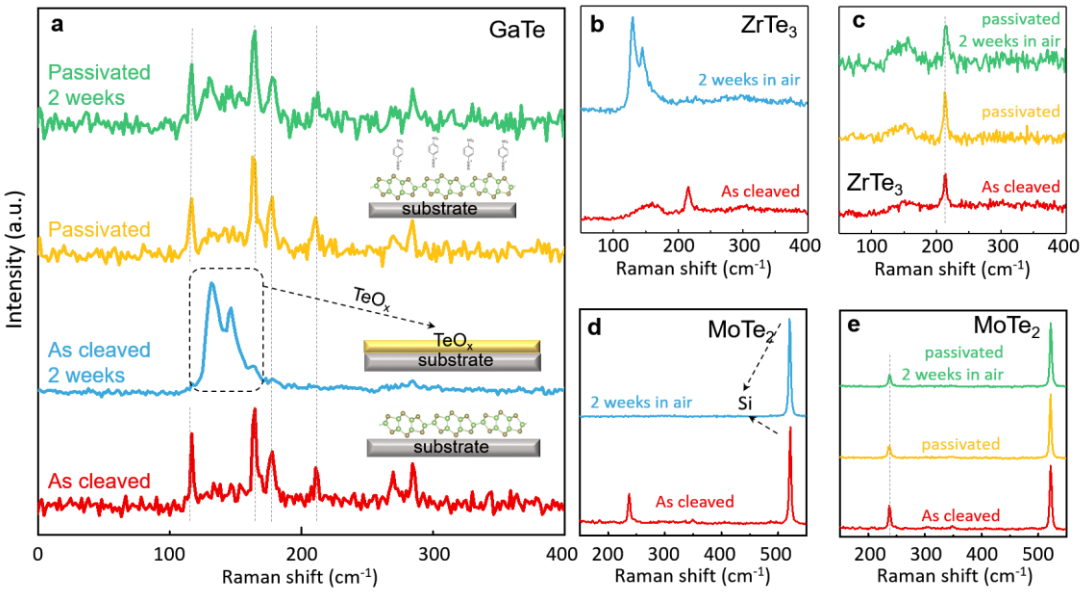

Figure 5.2 Effects of surface functionalization on GaTe, $ZrTe_3$, and $MoTe_2$. Raman spectra obtained from as-cleaved, aged, passivated, and passivated/aged (a) GaTe, (b, c) $ZrTe_3$, (d, e) $MoTe_2$.

We have also discovered that the same method is capable of enhancing material stability under extreme conditions. In a typical experiment, both surface functionalized and as-cleaved GaTe samples were immersed into deionized water for 5 hours and their Raman spectra were recorded before and after this process. As evidenced by the results shown in Figure 5.3a, as-cleaved GaTe sample without protection of diazonium molecules quickly transformed under water, whereas the surface functionalized sample showed only minimum changes, implying that material stability has been greatly enhanced (Figure 5.3b). In addition to 4-nitrobenzene diazonium tetrafluoroboride, we have also investigated the effect of 4-methoxybenzene diazonium tetrafluoroboride on these Te based 2D materials. Our results show that the two diazonium salts both improve the environmental stability of GaTe with no significant difference between them.

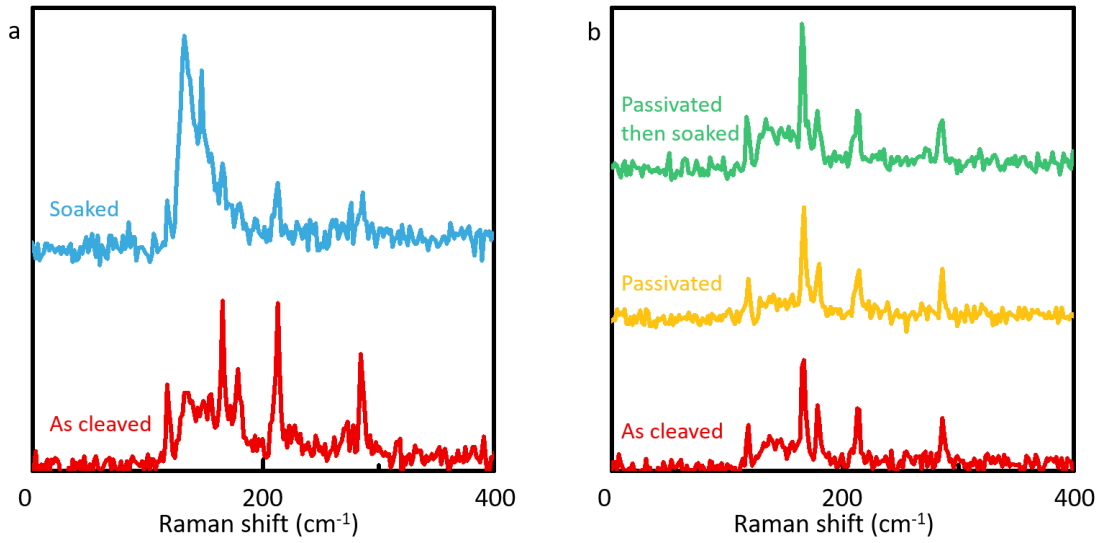

Figure 5.3 Enhanced stability of functionalized GaTe in water. (a) Raman spectra of as-cleaved GaTe before (red) and after immersing in water (blue). (b) Raman spectra of passivated GaTe before (yellow) and after immersing in water (green) compared to as-cleaved GaTe (red).

5.2.2 Effects on surface morphology

As mentioned in the previous chapter, environmental aging of GaTe causes detrimental effects on the surface of the material. AFM results show that the thickness of the material increases by ~5 nm and surface roughness increases by about 25% (Figure 5.4a-c). This increase in thickness can be attributed to the surface transformation of crystalline GaTe to amorphous tellurium oxide. In contrast, when we study the surface functionalization process with AFM, results show that thickness of the material increased by ~1 nm, which can be explained by the addition of one layer of diazonium molecules, while the surface roughness is relatively unchanged. Furthermore, after two weeks of aging in air, the surface functionalized sample still doesn't show any change in surface

roughness, whereas the thickness increased by ~1 nm (Figure 5.4d-f). The origin of this thickness increase is currently unknown and subject to further studies.

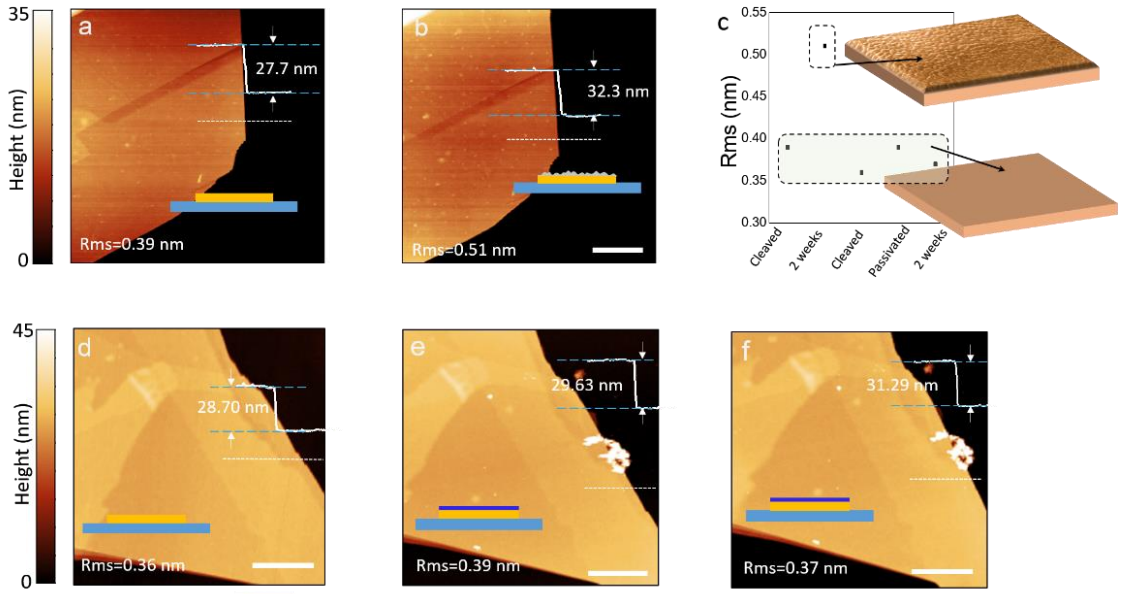

Figure 5.4 Surface morphology and thickness changes of GaTe during environmental aging. AFM images of (a) as-cleaved, (b) aged GaTe. (c) RMS roughness data calculated from different sample sets with schematic representation of the surfaces. (d) as-cleaved, (e) functionalized, and (f) aged-functionalized GaTe. Inset images depict surface transformation effects.

5.2.3 Unaffected physical properties

We note from the previous chapter that environmental aging causes GaTe to lose its anisotropic Raman response. Moreover, when the surface of GaTe undergoes transformation, the photoluminescence signal of GaTe is lost as well. Knowing that surface functionalization can effectively enhance the environmental stability of the material as evidenced by Raman spectroscopy, we have performed ARS and PL measurements to understand the effects of functionalization on material performance. PL

spectra collected from as-cleaved and functionalized samples suggest that PL intensity shows a ~50% decrease while the peak position and shape remain unchanged, which suggests that the optical bandgap of the material is not affected by surface functionalization (Figure 5.5a). On the other hand, the decrease of PL intensity could be associated with changes in radiative to non-radiative recombination timescales. As experimentally and theoretically predicted in the next section, electrons are withdrawn by surface aryl groups from the material which introduces p-type doping. In return, the increase of hole concentration stabilizes Auger non-radiative recombination process in which photons generated by electron-hole recombination transfer their energy to holes instead of generating radiative emission.

We also note that anisotropic material response is also lost as a result of surface deterioration evidenced by our ARS measurements. In contrast, surface functionalization inhibits this anisotropic to isotropic transition: the surface of functionalized GaTe remained highly anisotropic as shown in the polar Raman plot from Figure 5.5d-e, indicating that functionalization process itself didn't introduce any change in material anisotropy. Moreover, compared to non-functionalized GaTe samples which showed a circular plot after two weeks of aging, surface functionalized GaTe samples still showed strong anisotropic Raman response. This also proves that diazonium based surface functionalization is very effective in preventing gas/material interaction based surface transformation as well as anisotropic to isotropic transition.

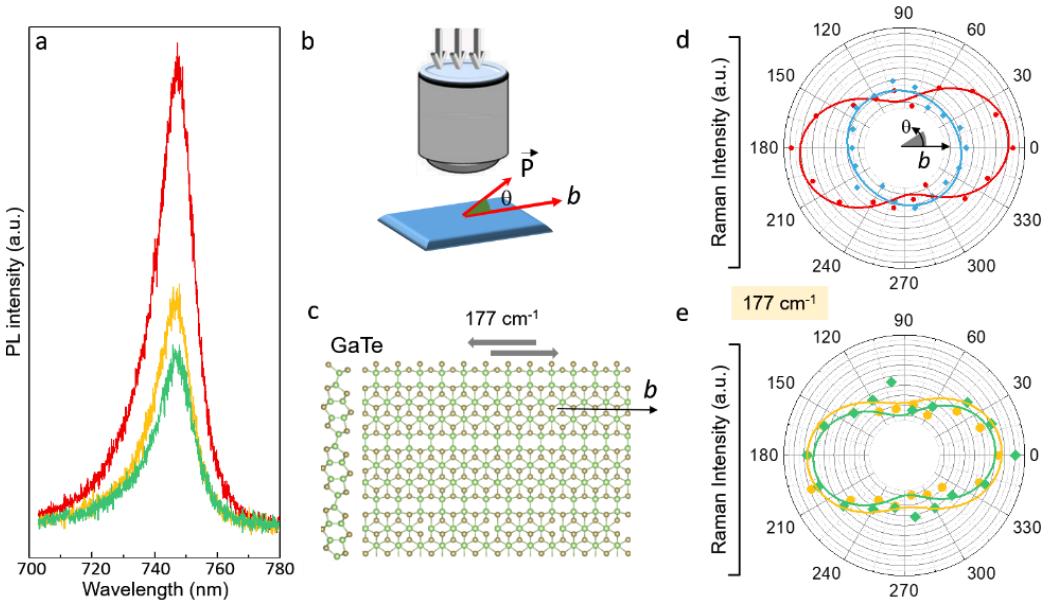

Figure 5.5 Effects of surface functionalization on physical properties of GaTe. (a) PL spectra of as-cleaved (red), passivated (yellow), and aged-passivated (green) GaTe. (b-c) Schematic description of angle resolved Raman spectroscopy and definition of polarization angle θ with respect to anisotropy axis and polarization direction. (c) Side and top view of monoclinic GaTe. (d) ARS data of 177 cm^{-1} peak for as-cleaved (red) and aged (blue) GaTe. (e) Polar plots of 177 cm^{-1} peak for passivated (yellow) and aged-passivated (green) GaTe.

Charge transfer induced by surface modification of molecular adsorption has been reported to affect the properties of 2D materials substantially[71]. Electron transfer between the dopant and material depends on their relative electronegativity. In the case of diazonium salt and GaTe, it is expected that the diazonium will be a p-type dopant[72, 73]. We have performed surface potential measurements through Kelvin probe force microscopy (KPFM) to understand the charge transfer at the GaTe/diazonium interface. GaTe was deposited onto a conductive indium tin oxide (ITO) surface by mechanical

exfoliation and surface potential measurements were performed before/after surface functionalization. As shown in Figure 5.6a, the surface potential of sample increased from 4.46 to 4.56 eV, meaning that the Fermi level of GaTe decreased by 100 meV as illustrated in the band diagram in Figure 5.6b. Our conductive AFM measurements (Figure 5.6d) on GaTe/ITO junctions also show that the I/V response remains largely unchanged while overall current decreases, which can be attributed to the presence of surface aryl groups on GaTe surface that results in tunnel barrier decreasing overall current.

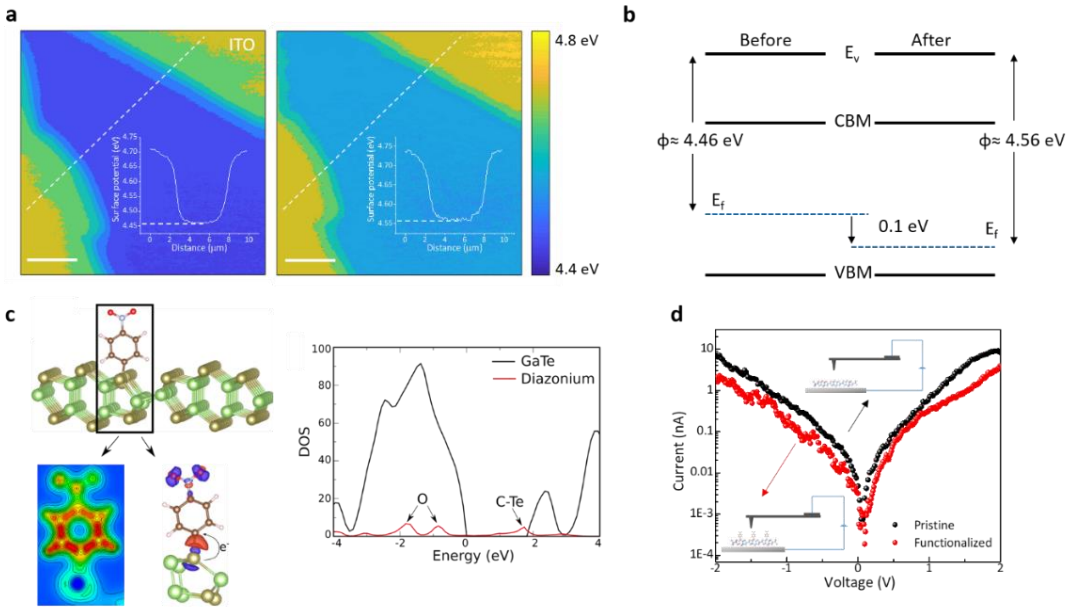

Figure 5.6 Electronic effects of surface aryl functionalization (a) Surface potential map before (left) and after (right) functionalization. (b) Band diagram of GaTe before/after functionalization. (c) DFT model and charge density map of surface functionalized GaTe. (d) I-V curves of as-cleaved (black) and functionalized (red) GaTe.

Our density functional theory (DFT) simulation results also clearly demonstrate that surface aryl groups withdraw electrons from tellurium sites in GaTe. During the

surface functionalization process, the N_2 dissociates from the diazonium molecule and a C-Te bond is established. In this configuration, electrons flow from Te to C, which renders the aryl functionalities a p-type dopant. We also note that this binding at the Te sites passivates the surface of GaTe which enhances material stability.

5.3 Summary

In summary, post-processing methods based on diazonium functionalization have proven to be an effective method to create environmentally stable GaTe, $ZrTe_3$, and $MoTe_2$ surfaces. While these materials are vulnerable to environmental degradation, diazonium molecules can effectively decorate their surfaces with aryl groups to enhance their stability in air as well as in water. Moreover, our spectroscopy and microscopy results suggest that the physical/chemical characteristics of the materials are not affected by surface functionalization as evidenced by unchanged optical bandgap, anisotropic response, and fixed PL emission wavelength. Surface potential measurements, along with DFT simulations, suggest diazonium molecules introduce p-type doping to GaTe by binding at the Te atoms on the surface. Our findings provide a way to significantly enhance the stability of Te containing 2D materials that are environmentally unstable through an inexpensive, reproducible, and manufacturing compatible surface chemical functionalization route.

CHAPTER 6

STABILITY OF HEXAAMINOBENZENE BASED 2D POLYMERS

6.1 Introduction to 2D polymers

The term polymer refers to macromolecule composed of many repeating units of smaller molecules, which are commonly organic molecules. Based on this definition, 2D polymer is a two-dimensional macromolecule with laterally connected repeating units[74-76]. Depending on the type of bonding between monomers, 2D polymers can be categorized into the following: covalent polymers, coordination polymers, and supramolecular polymers.

Compared to other 2D materials such as TMDC or PTMC, preparation of 2D polymers usually requires bottom-up synthesis due to their organic nature. This brings both advantages and disadvantages to 2D polymers. The advantage is that the structure of resulting 2D polymer can be easily modified by designing the structure of monomers that will be used for polymerization, which can be achieved with modern organic chemistry[77-80]. Meanwhile, an obvious disadvantage of 2D polymer is that material quality obtained from bottom-up synthesis is low. So far, research on 2D polymers have been mainly on the synthesis of such molecules while their physical properties are relatively unknown[74]. One type of 2D polymer based on transition metal ions coordinated by hexaaminobenzene (HAB) is of particular interest[81, 82]: all atoms within each layer of the polymer are in the same plane with their p/d orbitals overlapping, which can give rise to interesting electronic properties. The transition metal ions such as Ni and Co are also known to introduce magnetism. However, the building block, hexaaminobenzene, has been reported to undergo oxidation in air. This oxidation occurs on the amino groups

which are required for the formation of 2D framework with metal ions. For this reason, it is necessary to gain a good understanding of the stability of HAB based 2D polymer for the research of its physical properties.

6.2 Polymer synthesis

6.2.1 Synthesis of hexaaminobenzene

The polymer is the product between a direct reaction of HAB and a transition metal salt[81]. However, as HAB is not commercially available, it is necessary to synthesize it from simpler compounds. The synthesis of HAB has a well-established route with decent overall yield starting from 4-nitroaniline (PNA)[83, 84]. 4-nitroaniline first undergoes nitration with KNO_3 and H_2SO_4 to yield 2,4,6-trinitroaniline (TNA), followed by amination with 4-amino-4-H-1,2,4-triazole which yields (ATA) 2,4,6-triamino-1,3,5-trinitrobenzene (TATB). The last step involves the reduction of three nitro groups in TATB to yield HAB. Since HAB product will be used for the synthesis of 2D polymer with transition metal salt, reduction of nitro groups that involves metal or metal salts must be avoided. Therefore, phenylhydrazine is selected as the reducing agent for reduction of TATB[85]. The details of synthesis are described in the following section.

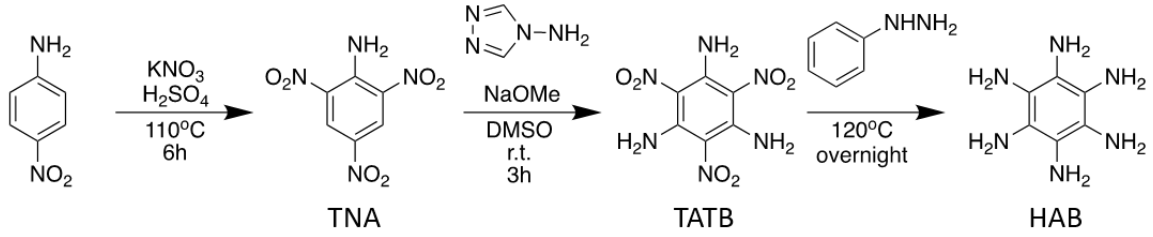

Figure 6.1 Synthesis scheme of Hexaaminobenzene.

6.2.1.1 Synthesis of TNA

In a typical experiment, 14g KNO_3 is dissolved in 20 ml concentrated H_2SO_4 and added to a pressure-equalizing dropping funnel. 4g 4-nitroaniline is dissolved in 20 ml concentrated H_2SO_4 and added to a 100 ml round bottom flask and the mixture is heated to 50^{o}C in an oil bath. The KNO_3 solution is then added dropwise to the 4-nitroaniline solution and the reaction is refluxed at 80^{o}C for 3h and then at 110^{o}C for 3h again. The reaction mixture is cooled in ice bath and slowly poured onto 20 grams of ice with vigorous stirring. The precipitate formed is collected by vacuum filtration and rinsed several times with DI water followed by drying in a vacuum oven, resulting in a brown powder (4.1g, 62% yield). The product is characterized by ^{1}HNMR and ^{13}CNMR. Results shown in figure 6.2 clearly demonstrate that the desired product is obtained in a pure form.

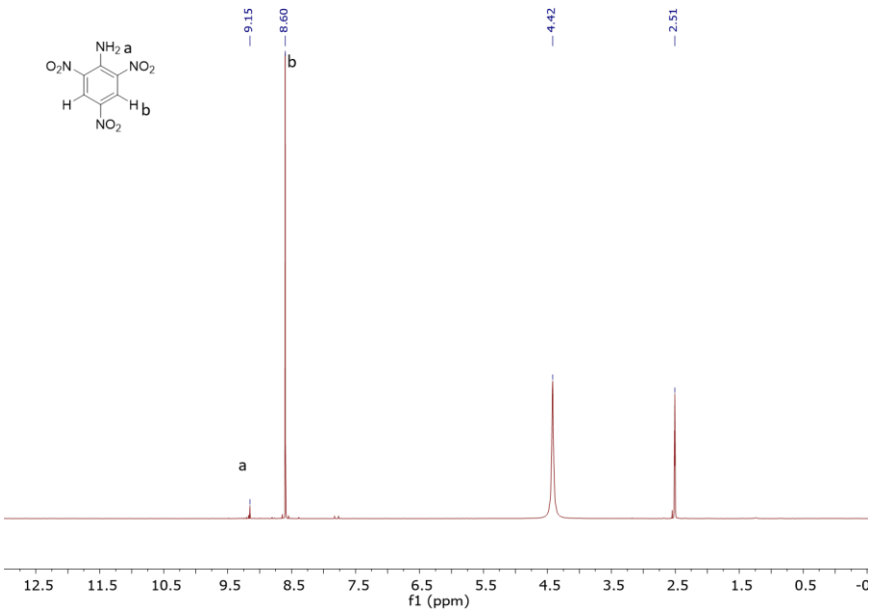

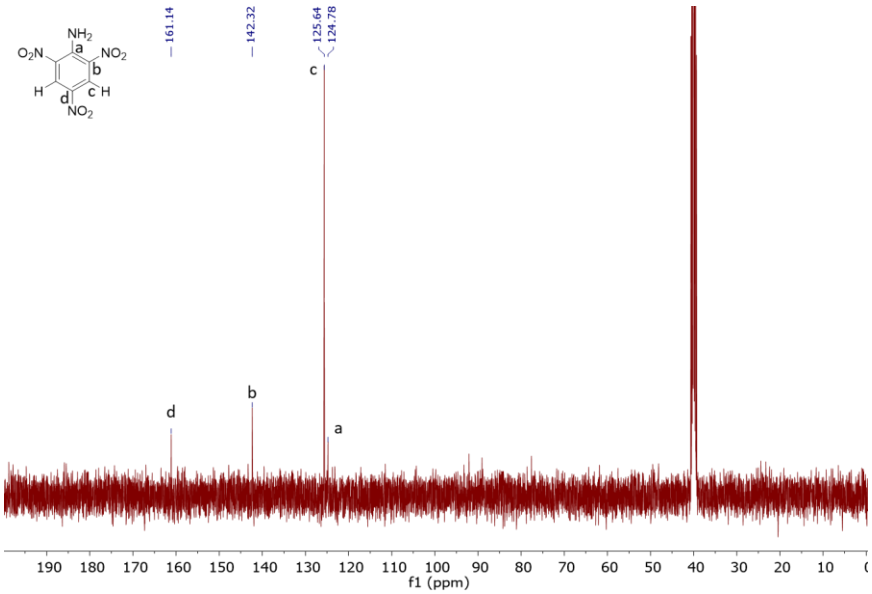

Figure 6.2 ^{1}HNMR (top) and ^{13}CNMR (bottom) of TNA in DMSO-d_6

6.2.1.2 Synthesis of TATB

1.2g NaOMe is dissolved in 5 mL dimethylsulfoxide (DMSO). 228mg TNA from previous step, 840mg ATA are dissolved in 10 ml DMSO at room temperature. The NaOMe solution is then slowly added to the TNA/ATA solution and the reaction is stirred at room temperature for 3h. The reaction mixture is then poured into 150 ml 0.4M HCl to crystallize the product. Resulting solid is then collected by vacuum filtration and rinsed with DI water. The dried crystals are fully dissolved in DMSO with a trace amount of NaOH. This mixture is then poured in cold dilute HNO3, and the precipitate is collected by filtration followed by vacuum drying to afford 195 mg (76% yield) of TATB as a dark brown powder. Characterization result from ^{13}CNMR shown in figure 6.3 demonstrates all four carbon signals from the product without any impurity peaks.

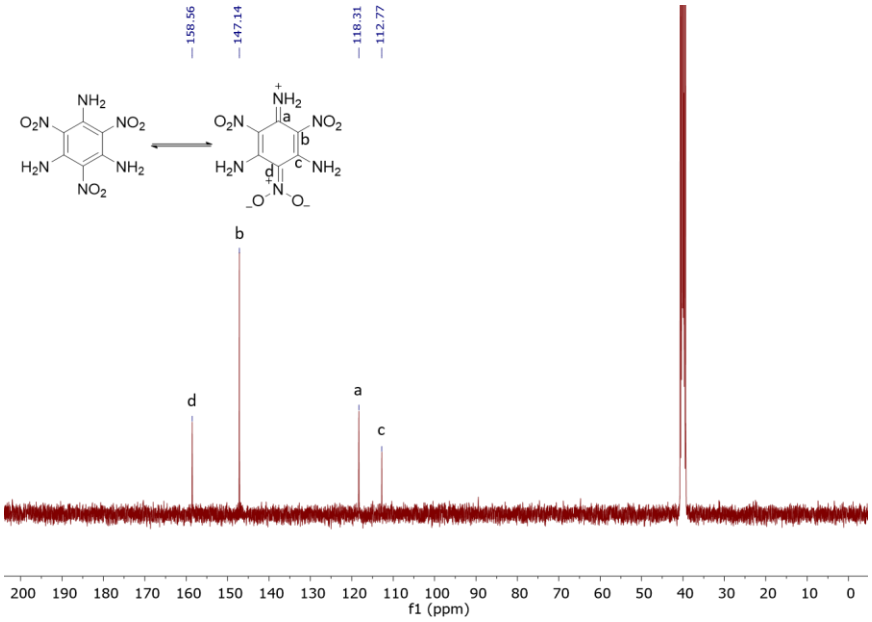

Figure 6.3 ^{13}CNMR of TATB in DMSO-d_6

6.2.1.3 Synthesis of HAB

26 mg TATB from the previous step is mixed 5 ml phenylhydrazine under N_2 atmosphere and refluxed overnight. After cooling to room temperature, the resulting mixture is poured into toluene to for crystallization and the precipitate is collected by vacuum filtration under N_2. The solid is then dissolved in DI water and insoluble impurities are filtered out. The filtrate is then free-dried to yield HAB as a dark brown solid. Product is characterized by ^{1}HNMR.

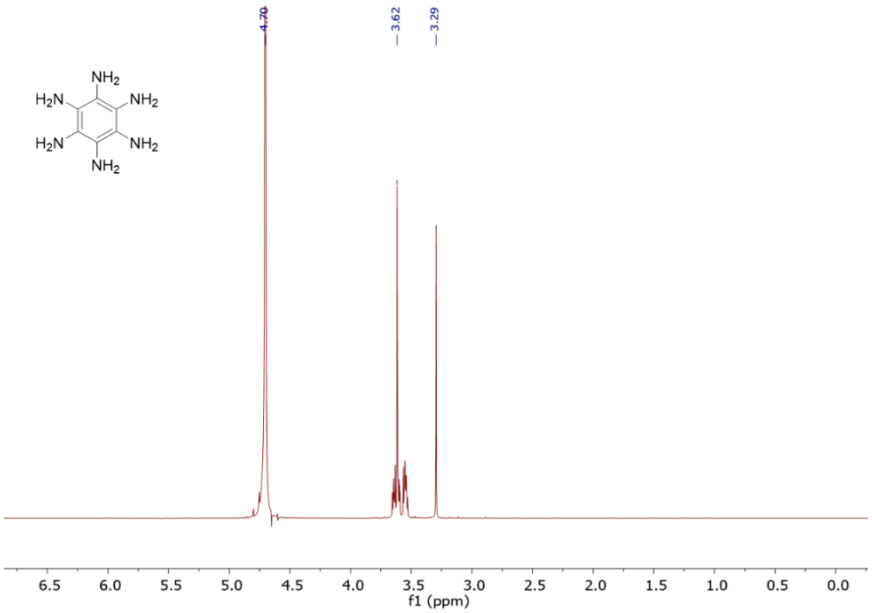

Figure 6.4 ^{1}HNMR of HAB in D_2O

6.2.2 Preparation of HAB based 2D polymer

The polymer is prepared by an interface reaction between HAB and organic salt of selected transition metals: $Ni(acac)_2$ and $Co(acac)_2$ in this case. In a typical synthesis, HAB is dissolved in O_2 free DI water and $M(acac)_2$ is dissolved in ethyl acetate (EtOAc) respectively and a small amount of $M(acac)_2$ solution is carefully added on top of the HAB solution. The reaction is then kept at room temperature for 4 hours. The polymer formed on the interface is then picked up with select wafer substrate (Si/SiO_2, sapphire, ITO, etc.). The deposited polymer sheets are then rinsed with DI water twice and dried under N_2 flow.

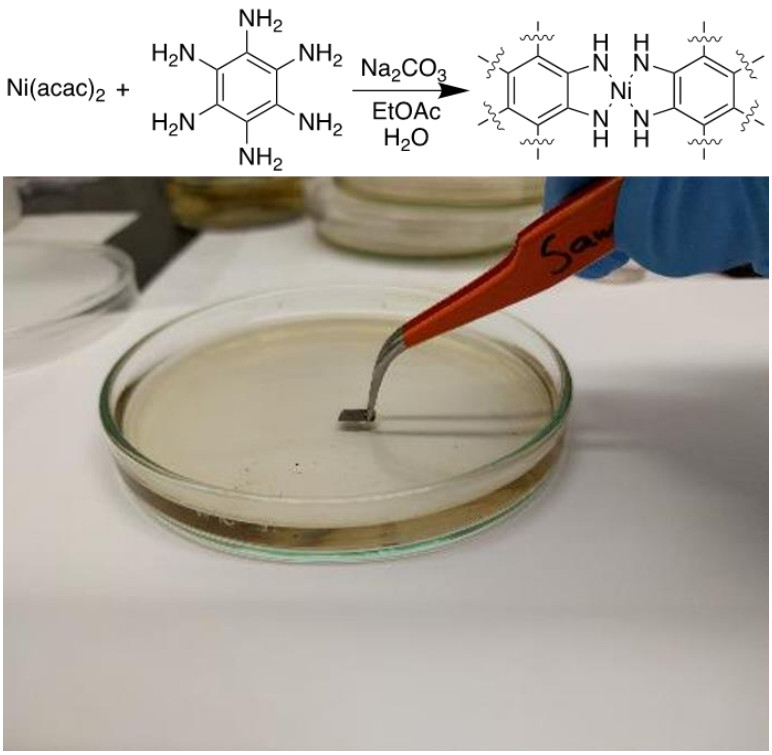

Figure 6.5 Schematics of 2D polymer synthesis

6.2.3 Characterization of HAB 2D polymer

The obtained polymer is first characterized to investigate its morphology. When viewed under optical microscope, samples appear as ribbon-like flakes, with lateral dimension of ~10 μm. AFM images recorded on the ribbon-like flakes show smooth surface (RMS roughness ~1.6 nm over a large area) with terrace structures, while the thickness of different samples ranges from 10 to 150 nm. However, holes are observed on some flakes under AFM, which is reasonable due to the bottom-up nature of the polymer synthesis. Scanning electron microscopy (SEM) images recorded near the edge of flakes demonstrate sharp edge and layered features. No significant difference is observed between Ni-HAB and Co-HAB, suggesting both metal precursors yield 2D polymer with same morphology. In summary, optical microscopy, along with AFM and SEM

demonstrate that the synthesized 2D polymer possess a certain degree of crystallinity and layered structure, although many defects are present.

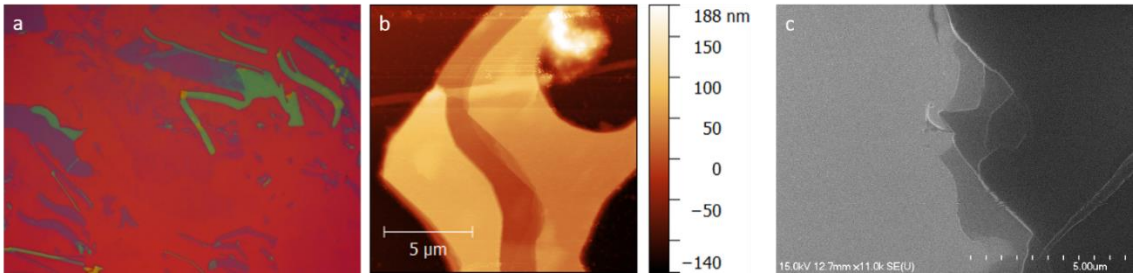

Figure 6.6 Morphology characterization of HAB based 2D polymer. (a) Optical image. (b) AFM image. (c) SEM image

Further characterization aimed at understanding the structure of formed polymer. Energy-dispersive X-ray spectroscopy (EDS) was first used to determine the elemental composition of the two polymers: Ni-HAB and Co-HAB. Results shown in figure 6.5 demonstrate that both polymers share characteristic peaks from C and O, while Ni-HAB sample possesses Ni signal and Co-HAB sample possesses Co signal respectively. N signal is not observed due to overlap with C signal. Raman spectroscopy and FTIR spectroscopy are then utilized to study the vibration properties of the 2D polymers. Both Ni-HAB and Co-HAB have same response in their Raman spectra as well as FTIR spectra, which is another indication that the crystal structure of the two polymers are same. In the Raman spectrum, two peaks at 1437.8 and 1460.3 cm^{-1} correspond to benzene ring stretch. In FTIR spectrum, the peak at 3176 cm^{-1} corresponds to the N-H stretch, and the peak at 1621.8 cm^{-1} corresponds to the C-C stretch in the benzene ring.

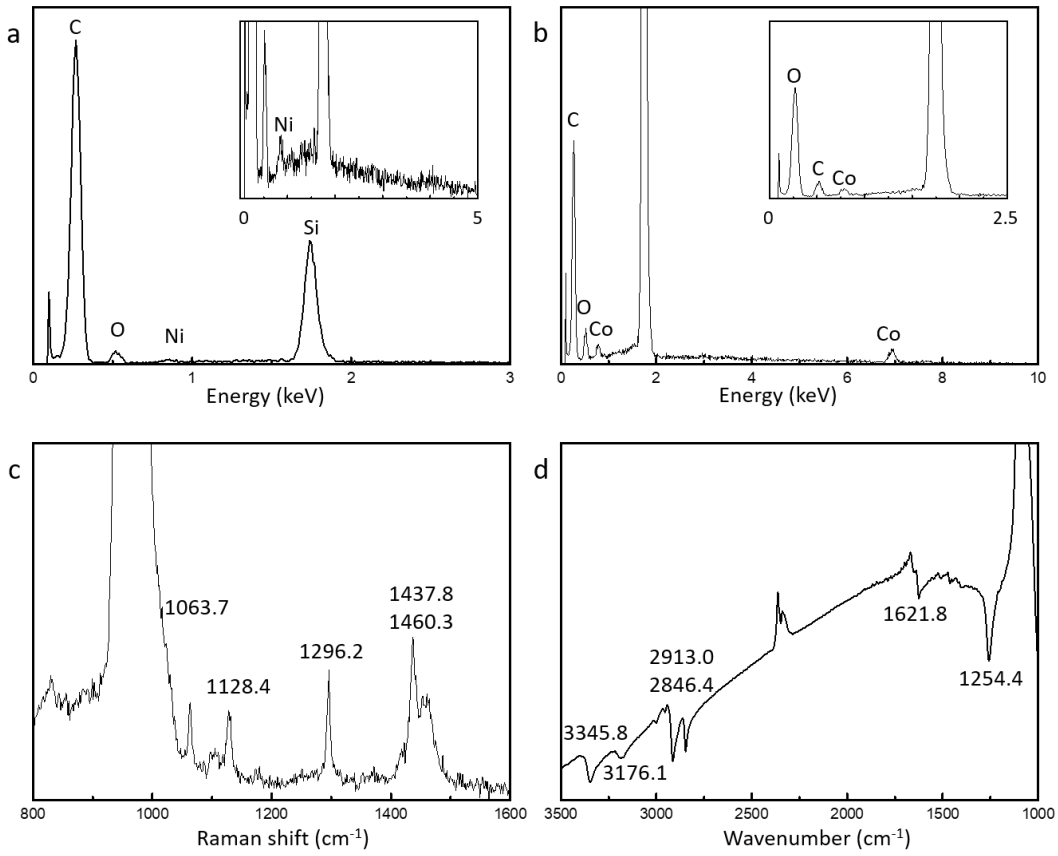

Figure 6.7 (a, b) EDX spectra of (a) Ni-HAB and (b) Co-HAB. Inset: zoom in. Raman spectrum (c) and FTIR spectrum (d) of M-HAB

Although the existing characterization results match with reported values, several critical results are still missing for unveiling the actual structure of M-HAB 2D polymer. Because of the reaction setup for the polymer growth, large crystal couldn't be obtained for X-ray crystallography. Transmission electron microscopy was attempted, but the sample underwent fast decomposition under electron beam so no reliable diffraction pattern was obtained.

6.3 Environmental stability of HAB 2D polymer

Degradation of Ni/Co-HAB was observed in some Raman spectroscopy measurements in which the sample at the laser spot disappeared after laser exposure. To understand the origin of polymer degradation, extensive conditional experiments were carried out.

6.3.1 Laser induced degradation

Since laser exposure in air is known to cause degradation of HAB based 2D polymers, various experiments are conducted to determine the factors that affect laser induced degradation. In these experiments, AFM is used to investigate minute surface morphology change caused by laser. The first finding is that there exists a power density threshold for the laser induced damage to occur. With a 488 nm blue laser, no damage is observed on the polymer sample if the power density of the laser is below 3×10^6 W/m^2. More laser sources with different wavelength are used to study the effect of laser wavelength, and results show green laser (533 nm) is more effective in inducing surface damage compared to blue laser, while red laser is less effective. The origin of this wavelength dependency is suspected to origin from different light absorption at different wavelengths, and is subject to further studies.

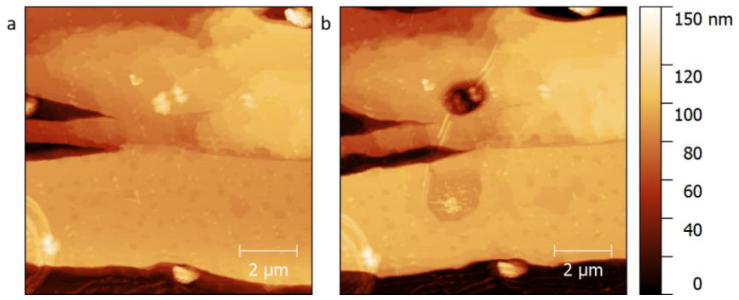

Figure 6.8 Laser induced degradation of HAB based 2D polymer. AFM scans before (a) and after (b) laser exposure.

6.3.2 Thermal stability

The effect of laser exposure is two-fold: it can heat up the sample locally as well as introducing photo-active surface species. Since both effects can result in material damage, it is necessary to distinguish the two effects to gain a better understanding of 2D polymer degradation mechanism. Thermal stability is then used as a simple yet effective test to determine whether degradation is thermal or light induced. To begin with, 2D polymer sample deposited on SiO_2/Si substrate is heated on a hotplate at 80 ℃ in air for 10 minutes. Surprisingly, all polymer flakes on the substrate disappeared after this process with little or no residue, implying that the 2D polymer has very low thermal stability. Further thermal stability experiments under different gas environments are performed in an environmental chamber equipped with a built-in heating unit: 2D polymer sample deposited on SiO_2/Si substrate is adhered on the heating unit with silver paste and the chamber is filled with a select type of gas. The temperature of the heating unit is then gradually increased while the optical image of the sample is constantly recorded during the process. When sample was heated in air, no thermal degradation is observed below 70 ℃, and then the sample started to decompose gradually between 70 and 80 ℃ (Figure 6.9). The same trend was observed in O_2 environment ($P_{O2} = 600\ Torr$), which suggests that oxygen could participate in the degradation process. In N_2 environment ($P_{N2} = 600\ Torr$), however, 2D polymer sample showed higher stability as degradation of sample started after heating to 120 ℃. Interestingly, if the nitrogen pressure is low (~100 mTorr) in the environmental chamber, sample degradation would still initiate at ~70 ℃. In another experiment, a 2D polymer sample stored in ambient condition at room temperature is found to slowly decompose over a week. Overall results

suggest that the degradation of M-HAB 2D polymer in air is a spontaneous process that can be accelerated by heat, where oxygen is likely involved in this process.

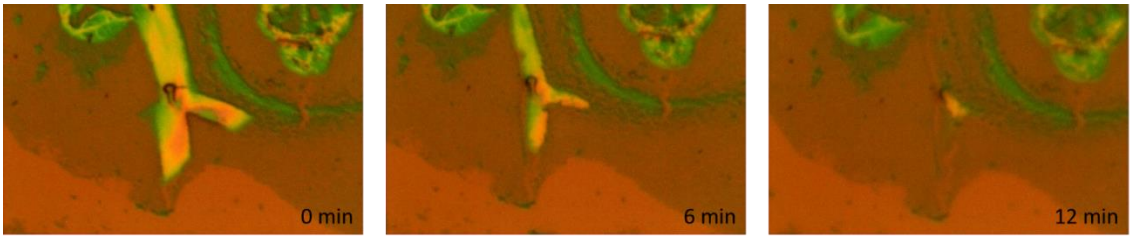

Figure 6.9 Optical images of HAB based 2D polymer during thermal degradation.

6.4 Future directions

6.4.1 Further understanding of polymer degradation

Although current experimental results suggest that the oxidation of HAB is very likely to cause degradation of the 2D polymer, there are a few questions need to be addressed: what is the exact mechanism that causes the oxidation of HAB and breakdown of 2D polymer framework? What is the residue after degradation? For the first question, better microscopy technique is required to study the morphology change of a sample *in situ*, preferably at atomic level resolution. Better conditional experiments can also be designed: for example, polymer sample can be encapsulated between the substrate and another material such as hexagonal boron nitride to inhibit the gas/material interaction. If the encapsulated sample demonstrates enhanced stability then it can be concluded that gas interaction is necessary for the degradation process. For the second question, determining the elemental composition of the residue through XPS or EDX will be the first step to solve it. Another approach to addressing this is to compare the TGA curves of HAB and M-HAB polymer in different gas environments.

6.4.2 Enhancing polymer stability

In order to enhance the stability of the M-HAB 2D polymer, there are several routes. One easy way to achieve this is to substitute HAB with other molecules that are capable of forming a 2D polymer but possess higher environmental stability. Another potential route is to use surface functionalization to passivate the surface of M-HAB 2D polymer to inhibit gas/material interaction to achieve higher environmental stability.

REFERENCES

1. Bhimanapati, G. R.; Lin, Z.; Meunier, V.; Jung, Y.; Cha, J.; Das, S.; Xiao, D.; Son, Y.; Strano, M. S.; Cooper, V. R.; Liang, L.; Louie, S. G.; Ringe, E.; Zhou, W.; Kim, S. S.; Naik, R. R.; Sumpter, B. G.; Terrones, H.; Xia, F.; Wang, Y.; Zhu, J.; Akinwande, D.; Alem, N.; Schuller, J. A.; Schaak, R. E.; Terrones, M.; Robinson, J. A. *ACS Nano* **2015,** 9, (12), 11509-11539.

2. Butler, S. Z.; Hollen, S. M.; Cao, L.; Cui, Y.; Gupta, J. A.; Gutiérrez, H. R.; Heinz, T. F.; Hong, S. S.; Huang, J.; Ismach, A. F.; Johnston-Halperin, E.; Kuno, M.; Plashnitsa, V. V.; Robinson, R. D.; Ruoff, R. S.; Salahuddin, S.; Shan, J.; Shi, L.; Spencer, M. G.; Terrones, M.; Windl, W.; Goldberger, J. E. *ACS Nano* **2013,** 7, (4), 2898-2926.

3. Novoselov, K. S.; Geim, A. K.; Morozov, S. V.; Jiang, D.; Zhang, Y.; Dubonos, S. V.; Grigorieva, I. V.; Firsov, A. A. *Science* **2004,** 306, (5696), 666-669.

4. Geim, A. K.; Novoselov, K. S. *Nature Materials* **2007,** 6, 183.

5. Andres, C.-G.; Leonardo, V.; Elsa, P.; Joshua, O. I.; Narasimha-Acharya, K. L.; Sofya, I. B.; Dirk, J. G.; Michele, B.; Gary, A. S.; Alvarez, J. V.; Henny, W. Z.; Palacios, J. J.; Herre, S. J. v. d. Z. *2D Materials* **2014,** 1, (2), 025001.

6. Li, L.; Yu, Y.; Ye, G. J.; Ge, Q.; Ou, X.; Wu, H.; Feng, D.; Chen, X. H.; Zhang, Y. *Nature Nanotechnology* **2014,** 9, 372.

7. Kim, K. K.; Hsu, A.; Jia, X.; Kim, S. M.; Shi, Y.; Dresselhaus, M.; Palacios, T.; Kong, J. *ACS Nano* **2012,** 6, (10), 8583-8590.

8. Ganatra, R.; Zhang, Q. *ACS Nano* **2014,** 8, (5), 4074-4099.

9. Lv, R.; Robinson, J. A.; Schaak, R. E.; Sun, D.; Sun, Y.; Mallouk, T. E.; Terrones, M. *Accounts of Chemical Research* **2015,** 48, (1), 56-64.

10. Zhang, Y.; Chang, T.-R.; Zhou, B.; Cui, Y.-T.; Yan, H.; Liu, Z.; Schmitt, F.; Lee, J.; Moore, R.; Chen, Y.; Lin, H.; Jeng, H.-T.; Mo, S.-K.; Hussain, Z.; Bansil, A.; Shen, Z.-X. *Nature Nanotechnology* **2013,** 9, 111.

11. Ellis, J. K.; Lucero, M. J.; Scuseria, G. E. *Applied Physics Letters* **2011,** 99, (26), 261908.

12. Zhao, W.; Ghorannevis, Z.; Chu, L.; Toh, M.; Kloc, C.; Tan, P.-H.; Eda, G. *ACS Nano* **2013,** 7, (1), 791-797.

13. Splendiani, A.; Sun, L.; Zhang, Y.; Li, T.; Kim, J.; Chim, C.-Y.; Galli, G.; Wang, F. *Nano Letters* **2010,** 10, (4), 1271-1275.

14. Buscema, M.; Steele, G. A.; van der Zant, H. S. J.; Castellanos-Gomez, A. *Nano Research* **2014,** 7, (4), 561-571.

15. Geim, A. K.; Grigorieva, I. V. *Nature* **2013,** 499, 419.

16. Wu, K.; Chen, B.; Yang, S.; Wang, G.; Kong, W.; Cai, H.; Aoki, T.; Soignard, E.; Marie, X.; Yano, A.; Suslu, A.; Urbaszek, B.; Tongay, S. *Nano Letters* **2016,** 16, (9), 5888-5894.

17. Wang, Q. H.; Kalantar-Zadeh, K.; Kis, A.; Coleman, J. N.; Strano, M. S. *Nature Nanotechnology* **2012,** 7, 699.

18. Ouyang, B.; Mi, Z.; Song, J. *The Journal of Physical Chemistry C* **2016,** 120, (16), 8927-8935.

19. Radisavljevic, B.; Radenovic, A.; Brivio, J.; Giacometti, V.; Kis, A. *Nature Nanotechnology* **2011,** 6, 147.

20. Sarkar, D.; Liu, W.; Xie, X.; Anselmo, A. C.; Mitragotri, S.; Banerjee, K. *ACS Nano* **2014,** 8, (4), 3992-4003.

21. Yu, Y.; Huang, S.-Y.; Li, Y.; Steinmann, S. N.; Yang, W.; Cao, L. *Nano Letters* **2014,** 14, (2), 553-558.

22. Yang, S.; Tongay, S.; Yue, Q.; Li, Y.; Li, B.; Lu, F. **2014,** 4, 5442.

23. Yang, S.; Wang, C.; Ataca, C.; Li, Y.; Chen, H.; Cai, H.; Suslu, A.; Grossman, J. C.; Jiang, C.; Liu, Q.; Tongay, S. *ACS Applied Materials & Interfaces* **2016,** 8, (4), 2533-2539.

24. Zhuang, H. L.; Hennig, R. G. *Chemistry of Materials* **2013,** 25, (15), 3232-3238.

25. Cai, H.; Soignard, E.; Ataca, C.; Chen, B.; Ko, C.; Aoki, T.; Pant, A.; Meng, X.; Yang, S.; Grossman, J.; Ogletree, F. D.; Tongay, S. *Advanced Materials* **2016,** 28, (34), 7375-7382.

26. Hui, C.; Jun, K.; Hasan, S.; Bin, C.; Aslihan, S.; Kedi, W.; Francois, P.; Xiuqing, M.; Sefaattin, T. *Nanotechnology* **2016,** 27, (6), 065203.

27. Cai, H.; Chen, B.; Wang, G.; Soignard, E.; Khosravi, A.; Manca, M.; Marie, X.; Chang, S. L. Y.; Urbaszek, B.; Tongay, S. *Advanced Materials* **2017,** 29, (8), 1605551-n/a.

28. Chen, B.; Sahin, H.; Suslu, A.; Ding, L.; Bertoni, M. I.; Peeters, F. M.; Tongay, S. *ACS Nano* **2015,** 9, (5), 5326-5332.

29. Ye, F.; Lee, J.; Hu, J.; Mao, Z.; Wei, J.; Feng, P. X. L. *Small* **2016,** 12, (42), 5802-5808.

30. Dai, J.; Li, M.; Zeng, X. C. *Wiley Interdisciplinary Reviews: Computational Molecular Science* **2016,** 6, (2), 211-222.

31. Kong, W.; Bacaksiz, C.; Chen, B.; Wu, K.; Blei, M.; Fan, X.; Shen, Y.; Sahin, H.; Wright, D.; Narang, D. S.; Tongay, S. *Nanoscale* **2017,** 9, (12), 4175-4182.

32. Wu, K.; Torun, E.; Sahin, H.; Chen, B.; Fan, X.; Pant, A.; Parsons Wright, D.; Aoki, T.; Peeters, F. M.; Soignard, E.; Tongay, S. **2016,** 7, 12952.

33. Zhang, X.; Tan, Q.-H.; Wu, J.-B.; Shi, W.; Tan, P.-H. *Nanoscale* **2016,** 8, (12), 6435-6450.

34. Lu, X.; Luo, X.; Zhang, J.; Quek, S. Y.; Xiong, Q. *Nano Research* **2016,** 9, (12), 3559-3597.

35. Beams, R.; Cançado, L. G.; Krylyuk, S.; Kalish, I.; Kalanyan, B.; Singh, A. K.; Choudhary, K.; Bruma, A.; Vora, P. M.; Tavazza, F.; Davydov, A. V.; Stranick, S. J. *ACS Nano* **2016,** 10, (10), 9626-9636.

36. Grzeszczyk, M.; Gołasa, K.; Zinkiewicz, M.; Nogajewski, K.; Molas, M. R.; Potemski, M.; Wysmołek, A.; Babiński, A. *2D Materials* **2016,** 3, (2), 025010.

37. Cançado, L. G.; Jorio, A.; Ferreira, E. H. M.; Stavale, F.; Achete, C. A.; Capaz, R. B.; Moutinho, M. V. O.; Lombardo, A.; Kulmala, T. S.; Ferrari, A. C. *Nano Letters* **2011,** 11, (8), 3190-3196.

38. Mignuzzi, S.; Pollard, A. J.; Bonini, N.; Brennan, B.; Gilmore, I. S.; Pimenta, M. A.; Richards, D.; Roy, D. *Physical Review B* **2015,** 91, (19), 195411.

39. Choi, J.-H.; Cui, P.; Lan, H.; Zhang, Z. *Physical Review Letters* **2015,** 115, (6), 066403.

40. Raja, A.; Chaves, A.; Yu, J.; Arefe, G.; Hill, H. M.; Rigosi, A. F.; Berkelbach, T. C.; Nagler, P.; Schüller, C.; Korn, T.; Nuckolls, C.; Hone, J.; Brus, L. E.; Heinz, T. F.; Reichman, D. R.; Chernikov, A. *Nature Communications* **2017,** 8, 15251.

41. Mark, D.; Viktor, Z.; Vladimir, I. F. k.; Igor, L. A. *2D Materials* **2016,** 3, (3), 035011.

42. Binnig, G.; Quate, C. F.; Gerber, C. *Physical Review Letters* **1986,** 56, (9), 930-933.

43. Giessibl, F. J. *Reviews of Modern Physics* **2003,** 75, (3), 949-983.

44. Paul, G. *Nanotechnology* **2001,** 12, (4), 485.

45. Coleman, J. N.; Lotya, M.; O'Neill, A.; Bergin, S. D.; King, P. J.; Khan, U.; Young, K.; Gaucher, A.; De, S.; Smith, R. J.; Shvets, I. V.; Arora, S. K.; Stanton, G.; Kim, H.-Y.; Lee, K.; Kim, G. T.; Duesberg, G. S.; Hallam, T.; Boland, J. J.; Wang, J. J.; Donegan, J. F.; Grunlan, J. C.; Moriarty, G.; Shmeliov, A.; Nicholls, R. J.; Perkins, J. M.; Grieveson, E. M.; Theuwissen, K.; McComb, D. W.; Nellist, P. D.; Nicolosi, V. *Science* **2011,** 331, (6017), 568-571.

46. Binnewies, M.; Glaum, R.; Schmidt, M.; Schmidt, P. *Zeitschrift für anorganische und allgemeine Chemie* **2013,** 639, (2), 219-229.

47. Pant, A.; Torun, E.; Chen, B.; Bhat, S.; Fan, X.; Wu, K.; Wright, D. P.; Peeters, F. M.; Soignard, E.; Sahin, H.; Tongay, S. *Nanoscale* **2016,** 8, (36), 16259-16265.
48. Zhang, Y.; Zhang, L.; Zhou, C. *Accounts of Chemical Research* **2013,** 46, (10), 2329-2339.

49. Lee, Y.-H.; Zhang, X.-Q.; Zhang, W.; Chang, M.-T.; Lin, C.-T.; Chang, K.-D.; Yu, Y.-C.; Wang, J. T.-W.; Chang, C.-S.; Li, L.-J.; Lin, T.-W. *Advanced Materials* **2012,** 24, (17), 2320-2325.

50. Liu, H.; Neal, A. T.; Zhu, Z.; Luo, Z.; Xu, X.; Tománek, D.; Ye, P. D. *ACS Nano* **2014,** 8, (4), 4033-4041.

51. Ling, X.; Wang, H.; Huang, S.; Xia, F.; Dresselhaus, M. S. *Proceedings of the National Academy of Sciences* **2015,** 112, (15), 4523-4530.

52. Tongay, S.; Sahin, H.; Ko, C.; Luce, A.; Fan, W.; Liu, K.; Zhou, J.; Huang, Y.-S.; Ho, C.-H.; Yan, J.; Ogletree, D. F.; Aloni, S.; Ji, J.; Li, S.; Li, J.; Peeters, F. M.; Wu, J. **2014,** 5, 3252.

53. Lin, Y.-C.; Komsa, H.-P.; Yeh, C.-H.; Björkman, T.; Liang, Z.-Y.; Ho, C.-H.; Huang, Y.-S.; Chiu, P.-W.; Krasheninnikov, A. V.; Suenaga, K. *ACS Nano* **2015,** 9, (11), 11249-11257.

54. Yang, S.; Tongay, S.; Yue, Q.; Li, Y.; Li, B.; Lu, F. *Scientific Reports* **2014,** 4, 5442.

55. Yang, S.; Wang, C.; Sahin, H.; Chen, H.; Li, Y.; Li, S.-S.; Suslu, A.; Peeters, F. M.; Liu, Q.; Li, J.; Tongay, S. *Nano Letters* **2015,** 15, (3), 1660-1666.

56. Dai, J.; Zeng, X. C. *Angewandte Chemie International Edition* **2015,** 54, (26), 7572-7576.

57. Island, J. O.; Biele, R.; Barawi, M.; Clamagirand, J. M.; Ares, J. R.; Sánchez, C.; van der Zant, H. S. J.; Ferrer, I. J.; D'Agosta, R.; Castellanos-Gomez, A. **2016,** 6, 22214.
58. Wu, K.; Torun, E.; Sahin, H.; Chen, B.; Fan, X.; Pant, A.; Parsons Wright, D.; Aoki, T.; Peeters, F. M.; Soignard, E.; Tongay, S. *Nature Communications* **2016,** 7, 12952.

59. Huang, S.; Tatsumi, Y.; Ling, X.; Guo, H.; Wang, Z.; Watson, G.; Puretzky, A. A.; Geohegan, D. B.; Kong, J.; Li, J.; Yang, T.; Saito, R.; Dresselhaus, M. S. *ACS Nano* **2016,** 10, (9), 8964-8972.

60. Lee, S.; Yang, F.; Suh, J.; Yang, S.; Lee, Y.; Li, G.; Sung Choe, H.; Suslu, A.; Chen, Y.; Ko, C.; Park, J.; Liu, K.; Li, J.; Hippalgaonkar, K.; Urban, J. J.; Tongay, S.; Wu, J. **2015,** 6, 8573.

61. Wang, X.; Jones, A. M.; Seyler, K. L.; Tran, V.; Jia, Y.; Zhao, H.; Wang, H.; Yang, L.; Xu, X.; Xia, F. *Nat Nano* **2015,** 10, (6), 517-521.

62. Duerloo, K.-A. N.; Li, Y.; Reed, E. J. **2014,** 5, 4214.

63. Balitskii, O. A.; Jaeckel, B.; Jaegermann, W. *Physics Letters A* **2008,** 372, (18), 3303-3306.

64. Gamal, G. A.; Nassary, M. M.; Hussein, S. A.; Nagat, A. T. *Crystal Research and Technology* **1992,** 27, (5), 629-635.

65. Briggs, D. *Surface and Interface Analysis* **1981,** 3, (4), v-v.

66. Balitskii, O. A.; Jaegermann, W. *Materials Chemistry and Physics* **2006,** 97, (1), 98-101.

67. Yang, S.; Cai, H.; Chen, B.; Ko, C.; Ozcelik, V. O.; Ogletree, D. F.; White, C. E.; Shen, Y.; Tongay, S. *Nanoscale* **2017,** 9, (34), 12288-12294.

68. Zhao, Q.; Wang, T.; Miao, Y.; Ma, F.; Xie, Y.; Ma, X.; Gu, Y.; Li, J.; He, J.; Chen, B.; Xi, S.; Xu, L.; Zhen, H.; Yin, Z.; Li, J.; Ren, J.; Jie, W. *Physical Chemistry Chemical Physics* **2016,** 18, (28), 18719-18726.

69. Lomeda, J. R.; Doyle, C. D.; Kosynkin, D. V.; Hwang, W.-F.; Tour, J. M. *Journal of the American Chemical Society* **2008,** 130, (48), 16201-16206.

70. Greenwood, J.; Phan, T. H.; Fujita, Y.; Li, Z.; Ivasenko, O.; Vanderlinden, W.; Van Gorp, H.; Frederickx, W.; Lu, G.; Tahara, K.; Tobe, Y.; Uji-i, H.; Mertens, S. F. L.; De Feyter, S. *ACS Nano* **2015,** 9, (5), 5520-5535.

71. Wang, H.; Yuan, H.; Sae Hong, S.; Li, Y.; Cui, Y. *Chemical Society Reviews* **2015,** 44, (9), 2664-2680.

72. Ryder, C. R.; Wood, J. D.; Wells, S. A.; Yang, Y.; Jariwala, D.; Marks, T. J.; Schatz, G. C.; Hersam, M. C. *Nat Chem* **2016,** 8, (6), 597-602.

73. Piazza, A.; Giannazzo, F.; Buscarino, G.; Fisichella, G.; Magna, A. L.; Roccaforte, F.; Cannas, M.; Gelardi, F. M.; Agnello, S. *The Journal of Physical Chemistry C* **2015,** 119, (39), 22718-22723.

74. Sakamoto, J.; van Heijst, J.; Lukin, O.; Schlüter, A. D. *Angewandte Chemie International Edition* **2009,** 48, (6), 1030-1069.

75. Colson, J. W.; Dichtel, W. R. *Nature Chemistry* **2013,** 5, 453.

76. Payamyar, P.; King, B. T.; Ottinger, H. C.; Schluter, A. D. *Chemical Communications* **2016,** 52, (1), 18-34.

77. Bieri, M.; Treier, M.; Cai, J.; Ait-Mansour, K.; Ruffieux, P.; Groning, O.; Groning, P.; Kastler, M.; Rieger, R.; Feng, X.; Mullen, K.; Fasel, R. *Chemical Communications* **2009**, (45), 6919-6921.

78. Weigelt, S.; Busse, C.; Bombis, C.; Knudsen, M. M.; Gothelf, K. V.; Lægsgaard, E.; Besenbacher, F.; Linderoth, T. R. *Angewandte Chemie International Edition* **2008,** 47, (23), 4406-4410.

79. Sun, Q.; Zhang, C.; Cai, L.; Xie, L.; Tan, Q.; Xu, W. *Chemical Communications* **2015,** 51, (14), 2836-2839.

80. Huang, X.; Sheng, P.; Tu, Z.; Zhang, F.; Wang, J.; Geng, H.; Zou, Y.; Di, C.-a.; Yi, Y.; Sun, Y.; Xu, W.; Zhu, D. *Nature Communications* **2015,** 6, 7408.

81. Lahiri, N.; Lotfizadeh, N.; Tsuchikawa, R.; Deshpande, V. V.; Louie, J. *Journal of the American Chemical Society* **2017,** 139, (1), 19-22.

82. Sakamoto, R.; Takada, K.; Pal, T.; Maeda, H.; Kambe, T.; Nishihara, H. *Chemical Communications* **2017,** 53, (43), 5781-5801.

83. Mahmood, J.; Kim, D.; Jeon, I.-Y.; Lah, M. S.; Baek, J.-B. *Synlett* **2013,** 24, (02), 246-248.

84. Breslow, R.; Maslak, P.; Thomaides, J. S. *Journal of the American Chemical Society* **1984,** 106, (21), 6453-6454.

85. Flurscheim, B.; Holmes, E. L. *Journal of the Chemical Society (Resumed)* **1929**, (0), 330-337.